RESEARCH ARTICLE

Key Points:
- Low-velocity zones produce dispersion curves with different shape than observed phase velocity
- High-velocity lid constrained to 200 km satisfies observations; without constraint, lid is 300 km
- For cratonic peridotite, Rayleigh waves require colder temperatures than xenolith thermobarometry

Supporting Information:
- Supporting Information S1
- Figure S1
- Figure S2
- Figure S3
- Figure S4
- Figure S5
- Figure S6
- Figure S7
- Figure S8
- Figure S9
- Figure S10
- Figure S11

Correspondence to:
A. C. Hirsch,
aaron_hirsch@uri.edu

Constraints on shear velocity in the cratonic upper mantle from Rayleigh wave phase velocity

Aaron C. Hirsch[1,2], Colleen A. Dalton[3], and Jeroen Ritsema[4]

[1]Department of Earth and Environment, Boston University, Boston, Massachusetts, USA, [2]Now at Graduate School of Oceanography, University of Rhode Island, Narragansett, Rhode Island, USA, [3]Earth, Environmental and Planetary Sciences, Brown University, Providence, Rhode Island, USA, [4]Department of Geological Sciences, University of Michigan, Ann Arbor, Michigan, USA

Abstract Seismic models provide constraints on the thermal and chemical properties of the cratonic upper mantle. Depth profiles of shear velocity from global and regional studies contain positive velocity gradients in the uppermost mantle and often lack a low-velocity zone, features that are difficult to reconcile with the temperature structures inferred from surface heat flow data and mantle-xenolith thermobarometry. Furthermore, the magnitude and shape of the velocity profiles vary between different studies, impacting the inferences drawn about mantle temperature and composition. In this study, forward modeling is used to identify the suite of one-dimensional shear-velocity profiles that are consistent with phase-velocity observations made for Rayleigh waves traversing Precambrian cratons. Two approaches to the generation of 1-D models are considered. First, depth profiles of shear velocity are predicted from thermal models of the cratonic upper mantle that correspond to a range of assumed values of mantle potential temperature, surface heat flow, and radiogenic heat production in the lithosphere. Second, shear velocity-depth profiles are randomly generated. In both cases, Rayleigh wave phase velocity is calculated from the Earth models, and acceptable models are identified on the basis of comparison to observed phase velocity. The results show that it is difficult but not impossible to find acceptable Earth models that contain a low-velocity zone in the upper mantle and that temperature structures that are consistent with constraints from mantle xenoliths yield phase-velocity predictions lower than observed. For most acceptable randomly generated Earth models, shear velocity merges with the global average at approximately 300 km.

1. Introduction

Continental crust contains the primary record of Earth's history beyond 200 Myr. The preservation of rocks in the continental crust is linked to the properties of the underlying lithospheric mantle: the long-term stability of the cratonic upper mantle has allowed for the long-term preservation of the continental crust. The fact that the continental lithosphere manages to avoid the fate of recycling suffered by oceanic lithosphere has been attributed to high viscosity and an intrinsic compositional buoyancy that offsets the negative thermal buoyancy imposed by the thick thermal boundary layer that exists beneath cratons [e.g., *Jordan*, 1975; *Hirth et al.*, 2000]. Both of these properties can be achieved if the lithospheric mantle has experienced very high degrees of partial melting and subsequent melt removal [*Jordan*, 1978; *Carlson et al.*, 2005], and over the past few decades the prevailing notion of the Precambrian continental lithosphere has been as a thick boundary layer (200–300 km) with a depleted peridotite composition and temperature structure controlled by steady state conductive cooling.

Seismological models provide important constraints on the properties of the cratonic upper mantle. Global seismic models show clearly that the cratonic upper mantle is characterized by higher wave speeds than noncratonic mantle to depths of at least 200 km [e.g., *Kustowski et al.*, 2008; *Ritsema et al.*, 2011; *Lekic and Romanowicz*, 2011a; *Jordan and Paulson*, 2013]. The difference in shear velocity at 100 km depth between mid-ocean ridges and cratons is 8–10%, depending on the choice of seismic model; at 200 km the difference is 3–5%. Comparison of regional seismic models from cratonic and oceanic settings reveals shear-velocity differences that are similar to, and in some cases more pronounced than, the global models [e.g., *Nishimura and Forsyth*, 1989; *Fishwick et al.*, 2005; *Chen et al.*, 2007; *Yang et al.*, 2007; *Darbyshire and Eaton*, 2010]. Without a doubt, the large contrast in upper mantle temperature between the two settings
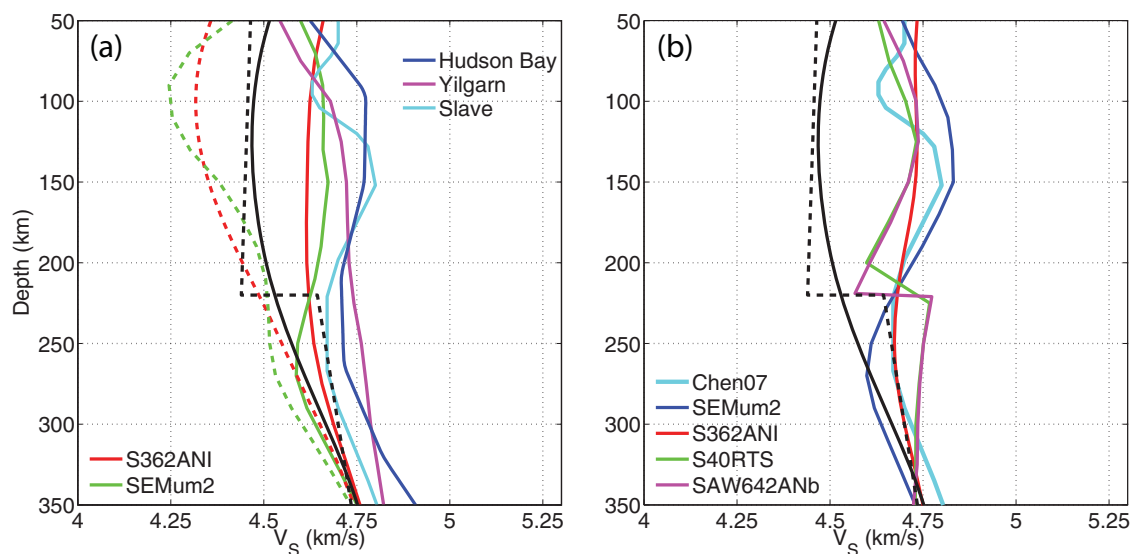
Figure 1. (a) Red and green curves show Voigt-averaged isotropic shear velocity from global models S362ANI [*Kustowski et al.*, 2008] and SEMum2 [*French et al.*, 2013]; dashed curves represent a global average beneath seafloor <25 Myr and solid curves are a global average beneath Archean cratons. Regional V_S models beneath cratons are shown for Hudson Bay [*Darbyshire and Eaton*, 2010], Yilgarn [*Fishwick et al.*, 2005], and Slave [*Chen et al.*, 2007]. One-dimensional reference models PREM [*Dziewonski and Anderson*, 1981] and STW105 [*Kustowski et al.*, 2008] are plotted with dashed and solid black, respectively. (b) Comparison of isotropic shear velocity beneath Slave craton (64°N, 110°W) from *Chen et al.* [2007] and global models SEMum2, S362ANI, S40RTS [*Ritsema et al.*, 2011], and SAW642ANb [*Panning and Romanowicz*, 2006].

contributes significantly to the observed large contrast in shear velocities; furthermore, it is likely that the depleted composition [e.g., *Jordan*, 1979; *Goes et al.*, 2000; *Lee*, 2003; *Schutt and Lesher*, 2006; *Dalton and Faul*, 2010] of the cratonic lithosphere further elevates shear velocity.

Two aspects of shear-velocity structure from cratons are particularly valuable for our understanding of the structure in these regions. The magnitude of shear velocity places bounds on the plausible range of temperatures and compositions, and the shape of the profiles as a function of depth constrains the thermal and chemical gradients. For example, it is well established that shear velocity beneath the oceans depends on seafloor age, with higher velocity and a deeper low-velocity zone (LVZ) beneath older seafloor [e.g., *Nishimura and Forsyth*, 1989; *Gaherty and Dunn*, 2007]. The higher velocity indicates lower temperatures at a given depth, and the deeper LVZ can be attributed to joining of the conductively cooling lid with the mantle adiabat at greater depths [*Faul and Jackson*, 2005; *Stixrude and Lithgow-Bertelloni*, 2005]. While these two properties are not independent—colder temperature produces a thicker lid, which necessitates a deeper intersection with the adiabat—consideration of both of them strengthens the interpretation.

Examples of shear-velocity profiles beneath cratons from global and regional studies (Figure 1) highlight several perplexing features. One, these profiles are characterized by positive or zero velocity gradients with depth in the uppermost mantle. Two, most profiles lack a low-velocity zone, in sharp contrast to profiles beneath the seafloor. This is noteworthy because predictions of shear velocity in a thermal boundary layer with uniform peridotite composition require a negative velocity gradient and LVZ as a result of the large positive vertical temperature gradient in the overlying conductive layer and the transition to an adiabatic temperature gradient [e.g., *Bruneton et al.*, 2004a; *Shapiro and Ritzwoller*, 2004; *Faul and Jackson*, 2005; *Stixrude and Lithgow-Bertelloni*, 2005]. Three, the cratonic profiles contain very high shear wave speed (4.7–4.8 km/s) in the shallow mantle; any model describing the thermal and chemical structure of cratons must be consistent with these values. Four, the details of the magnitude and shape of cratonic shear-velocity profiles vary between different studies (Figure 1b). Indeed, the variability between models for the Slave craton (sampled at 64°N, 110°W in the global models) is nearly as large as the variability in global averages (Figure 1a), and attempts to infer the thermal and chemical properties of cratons will yield different conclusions from different studies.

These intriguing aspects of the shear-velocity structure beneath cratons have been observed and investigated by earlier studies. Flat or positive velocity gradients with depth and the absence of a low-velocity zone have been noted in the central Baltic Shield [*Bruneton et al.*, 2004a, 2004b; *Zhu and Tromp*, 2013], the

East European craton [*Zhu and Tromp*, 2013], and central Australia [*Fishwick and Reading*, 2008]. In the Slave craton, *Chen et al*. [2007] image a minor velocity reduction around 100 km depth but do not consider it a robust feature, given its sensitivity to the level of damping. Velocity profiles determined from interstation dispersion curves in the Hudson Bay contain a slight low-velocity zone at approximately 250 km [*Darbyshire and Eaton*, 2010]. Models derived from two-station Rayleigh wave measurements in the Superior Province also contain a low-velocity zone, although the magnitude and depth of this feature are more variable across the study region [*Darbyshire et al*., 2007]. Surface-wave studies of southern Africa and the Kaapvaal craton have been inconclusive regarding the presence of a low-velocity zone. *Li and Burke* [2006] found a low-velocity zone centered near 250 km; it is a weaker feature than the low-velocity zone imaged by *Weeraratne et al*. [2003] beneath Tanzania, but the Rayleigh wave phase velocities cannot be fit without it. *Priestley et al*. [2006] also identify a low-velocity zone at 200–250 km whereas *Larson et al*. [2006] find that such a velocity reduction is incompatible with their Rayleigh wave dispersion data for the Kaapvaal craton.

Two studies have sought to bridge the resolution gap between global tomographic models and regional studies by considering simultaneously and treating in a consistent fashion several cratonic areas. *Pedersen et al*. [2009] compiled dispersion curves from the literature for the Archean Kaapvaal, Slave, and Yilgarn cratons and the Archean/Proterozoic South-Central Finland. A single Rayleigh wave dispersion curve, with error bars, was constructed for each region in the approximate period range 20–170 s. While there is considerable overlap between the four curves, Yilgarn and Kaapvaal stick out as anomalously fast at shorter periods and slow at longer periods, respectively. The Slave, Yilgarn, and Finland dispersion curves can all be matched by an Earth model containing constant shear velocity from the Moho to 220 km, whereas Kaapvaal requires a decrease in velocity. The authors are unable to find a satisfactory explanation for why models containing a low-velocity zone cannot match the observations and conclude that their findings "reveal a major gap in our understanding of the structure of the cratonic lithosphere."

Lebedev et al. [2009] identified 10 pairs of seismic stations located on Archean and Proterozoic crust and measured interstation phase velocity for fundamental-mode Rayleigh and Love waves. The shear-velocity profiles that fit these data are consistently found to contain increasing shear velocity from the Moho to 150 km; a decrease in shear velocity at depths >150 km is favored by the observations in only a handful of locations. The authors attribute the velocity increase with depth to a spinel-garnet transition that is distributed over a broad depth interval, although they do not demonstrate whether such a compositionally induced increase is large enough to offset the thermally induced velocity decrease that would be prominent within a thermal boundary layer.

Indeed, only a relatively small number of studies have rigorously considered the implications that the seismic properties of the cratonic upper mantle have on its thermal and chemical properties, and how these estimated properties compare with other available constraints, for example, from xenolith samples and surface heat flow. *Shapiro and Ritzwoller* [2004] and *Shapiro et al*. [2004] assimilated heat flow data into their inversion of surface-wave dispersion and showed that doing so reduces the range of acceptable seismic models, especially in cratonic areas. This approach tends to eliminate seismic models containing a positive velocity gradient in the shallow mantle, because those models require a negative temperature gradient that is incompatible with the heat flow observations. The impact of this model selection on the fit to the observations is not discussed in detail in these papers. *Bruneton et al*. [2004a] computed shear velocity-depth profiles for nine different mantle compositions along a geotherm that is consistent with xenolith thermobarometry in the Baltic Shield. All nine profiles contain a negative velocity gradient that terminates in a distinct low-velocity zone at 250 km; the observed profiles, on the other hand, have a slightly positive gradient and no low-velocity zone. Furthermore, the predicted velocities for a peridotite composition are much higher than observed at depths <160 km. The authors conclude that the shallow mantle must be comprised of rocks more exotic than pure peridotite—perhaps 60% residue from granitoid formation and 40% harzburgite. *Darbyshire and Eaton* [2010] tested three compositional models and adjusted the mantle temperature profile to obtain Rayleigh wave phase velocity that agrees with the observed values for Hudson Bay. Although they are able to satisfy the observations with a constant-composition mantle, doing so requires temperatures in the shallow mantle that are much colder than estimates from cratonic mantle xenoliths and conductive geotherms that join the adiabat at depths >300 km. *Afonso et al*. [2013a, 2013b] have developed a probabilistic method that combines several types of geophysical observables to constrain the thermal and compositional structure of the lithosphere. This approach couples an internally consistent

thermodynamic formalism with compositional parameters determined from large databases of natural mantle samples. It has been applied to seismic, geoid, topographic, and heat flow data from South China to estimate variations in lithospheric thickness and composition [*Shan et al.*, 2014].

In this paper, we aim to characterize the average properties of the cratonic upper mantle on a global scale. Like *Lebedev et al.* [2009] and *Pedersen et al.* [2009], we want to consider simultaneously and treat in a consistent fashion several different cratonic settings, and we want our analysis to be based on the surface-wave dispersion curves rather than on tomographic models, which contain the effects of parameterization and regularization. Here our analysis is focused on the global average; we will present a comparison of different cratonic regions in a subsequent publication. We use the global data set of Rayleigh wave phase velocity from *Ritsema et al.* [2011] in the period range 40–235 s and consider a regionalization of global cratons that provides a more complete sampling of cratonic regions than the earlier studies (supporting information Figure S1). We use forward modeling to identify the suite of 1-D Earth models that are compatible with phase-velocity observations for Rayleigh waves traversing cratons. As described below, our model-space search is very broad. It allows us to explicitly test for the presence of certain features, for example positive velocity gradients, low-velocity zones, and high shear wave speeds. It also allows us to control factors such as the crustal thickness and the ratio of compressional velocity to shear velocity, on which the Rayleigh wave phase velocity depends, and more easily test the sensitivity of our results to assumptions about these factors than is possible when using inverse methods. Finally, we seek to understand what temperature profiles are implied by the suite of acceptable models and to what extent those temperatures are consistent with the constraints provided by cratonic mantle xenoliths. For this step we use thermodynamic calculations performed by the software package PerpleX [*Connolly*, 2009] in order to most accurately compute the effect of temperature and composition on elastic shear velocity.

One-dimensional Earth models are calculated using two approaches, and the predicted phase velocity for each model is compared to the observed range to identify models that provide a satisfactory fit to the observations. The first approach recognizes that data sets other than seismic models provide constraints on the temperature and composition of the cratonic upper mantle. We generate cratonic geotherms for a range of surface heat flow, crustal-thickness, and radiogenic heat-production values, and shear velocity is calculated from the geotherms. Observations of surface heat flowing out of cratons are low and fairly uniform (41 ± 12 mW/m^2) [*Rudnick et al.*, 1998]; however, uncertainties in the amount of radiogenic heat production and in the value of thermal conductivity permit a wide variety of temperature structures to be inferred from surface heat flow data [*Rudnick and Nyblade*, 1999; *Shapiro and Ritzwoller*, 2004; *Hieronymus and Goes*, 2010]. In addition to surface heat flow, thermobarometry performed on mantle xenoliths has generated temperature estimates for the lithosphere beneath several Archean cratons, assuming that xenoliths record the temperature conditions of the present-day mantle [e.g., *Boyd et al.*, 1997; *Rudnick and Nyblade*, 1999; *Kopylova and Russell*, 2000; *Lee et al.*, 2011]. With the second approach, profiles of shear velocity are generated using random perturbations to the global reference model STW105 [*Kustowski et al.*, 2008]. This approach allows us to search for velocity profiles that are compatible with the seismological observations but whose shape and magnitude may deviate from what is expected for a simple thermal boundary layer with uniform composition. In total, 26,250 geotherm-generated and 80,000 randomly generated 1-D Earth models are compared to the observations in order to identify the suite of acceptable Earth models.

With this suite of Earth models, we wish to address a number of questions, including: (i) Is it possible to find an acceptable Earth model containing a low-velocity zone, as expected for a thermal boundary layer of uniform composition, or do all acceptable Earth models have features similar to those in Figure 1? (ii) Assuming a depleted peridotite composition, what temperature structures are inferred from the acceptable Earth models and how do these temperature profiles compare to temperature constraints provided by surface heat flow and xenolith thermobarometry?

It is tempting to also use our analysis to constrain the depth to which the cratonic lithosphere extends. However, doing so is not straightforward, as the criteria used to define the seismological signature of the lithosphere and its base vary from study to study. *Eaton et al.* [2009] provide a comprehensive review of the various approaches employed, which include specific characteristics of the shape and/or magnitude of shear-velocity profiles; changes in azimuthal anisotropy with depth; the presence or absence of radial anisotropy; and receiver functions. A number of recent seismic studies have estimated the base of the cratonic lithosphere at approximately 200–250 km [e.g., *Chen et al.*, 2007; *Yuan and Romanowicz*, 2010; *Lekic and*

Table 1. Summary of Rayleigh Wave Data Set, the Center of the Phase-Velocity Range as Determined by Pure-Path Inversion of the Whole Data Set, and the Observed Range of Phase Velocity that Characterizes Cratons

Period (s)	Total No. of Paths	Paths With >60% Length in Cratons	Craton Pure-Path Phase Velocity (km/s)	Observed Cratonic Phase-Velocity Range (km/s)
40	1,147,255	271	4.03	3.98–4.09
43	1,123,660	260	4.06	4.00–4.12
47	1,108,743	262	4.09	4.02–4.15
51	1,090,418	253	4.11	4.04–4.18
56	1,062,558	243	4.14	4.06–4.21
62	1,042,224	224	4.16	4.09–4.24
69	1,018,652	200	4.19	4.11–4.26
78	998,622	180	4.21	4.14–4.28
88	957,877	163	4.23	4.17–4.29
100	900,336	151	4.25	4.19–4.32
114	808,183	124	4.29	4.23–4.35
131	681,210	99	4.34	4.28–4.40
151	547,943	80	4.41	4.35–4.46
174	410,816	52	4.51	4.46–4.55
202	286,898	35	4.63	4.59–4.68
235	181,556	17	4.84	4.80–4.88

Romanowicz, 2011b]. *Jordan and Paulson* [2013] determined the depths of convergence of shear velocity in different tectonic provinces using 21 global tomographic models and found that shear velocities beneath stable cratons and mature ocean basins remain distinct to depths >350 km, suggesting very thick continental keels. While a thorough investigation of the surface-wave constraints on cratonic lithospheric thickness is beyond the scope of this study, we do evaluate randomly generated Earth models, systematically varying the maximum allowable depth of the random perturbation. On the basis of the acceptable randomly generated Earth models identified by this study, we can therefore comment on the depth to which shear velocities remain elevated above the global average, but we defer to a subsequent publication the inferences that can be drawn from these results about the thickness of the continental lithosphere.

2. Data

The data used in this study are path-averaged phase velocities of fundamental-mode Rayleigh waves at 16 discrete periods ranging from 40 to 235 s. The data are obtained from the global data set of *Ritsema et al.* [2011]. The peak sensitivity to shear velocity of fundamental-mode Rayleigh waves with 40 s period occurs at ∼50 km depth; for 235 s Rayleigh waves the peak sensitivity is distributed over the depth range 300–500 km. We seek to determine, at each period, the phase-velocity range that is characteristic of cratons on a global scale. Ideally, we would be able to characterize the phase-velocity range of cratons using a large number of Rayleigh wave paths that travel exclusively, from source to station, through cratons, providing complete and even coverage beneath Archean crust across the globe. However, such data are virtually non-existent, and we must extract information on cratonic phase velocity from Rayleigh wave paths that travel through other tectonic settings in addition to cratons. Approaches for isolating the cratonic signal in teleseismic Rayleigh wave paths include the two-station approach [e.g., *Darbyshire et al.*, 2007; *Lebedev et al.*, 2009], the two-plane-wave approach [e.g., *Weeraratne et al.*, 2003; *Li and Burke*, 2006], and embedding a high-resolution regional model within a global model [e.g., *Yuan et al.*, 2014]. Since we are interested in characterizing the average properties of the cratonic upper mantle on a global scale, we utilize a pure-path inversion approach applied to a large global data set of Rayleigh wave phase measurements [*Ritsema et al.*, 2011] (Table 1 and supporting information Figure S1). We prefer to use the raw observations rather than existing global phase-velocity maps because the tomographic phase-velocity values may be affected by choices about damping, parameterization, and theory.

At each period the cratonic phase-velocity range is defined by a center value and a width. We determine the center of the phase-velocity range using a pure-path inversion approach, in which the surface of the Earth is divided into six tectonic regions using the GTR1 tectonic regionalization [*Jordan*, 1981]. Regions A, B, and C indicate young (0–25 Myr), intermediate-age (25–100 Myr), and old (>100 Myr) seafloor, respectively. Regions P, Q, and S indicate continental areas classified by tectonic history:

Phanerozoic platforms, orogenic regions, and Precambrian cratons, respectively. The GTR1 regionalization scheme (supporting information Figure S1a) has been utilized in numerous earlier global studies of the cratonic lithosphere [e.g., *Shapiro et al.*, 1999; *Rychert and Shearer*, 2009; *Khan et al.*, 2011; *Jordan and Paulson*, 2013]. At each angular frequency ω, the global data set of path-averaged phase-velocity anomalies for earthquake i and station j is used to determine a representative phase-velocity anomaly dc_n/c for each region:

$$\overline{\frac{dc_{ij}}{c}}(\omega) = X_{ij}^A \frac{dc_A}{c}(\omega) + X_{ij}^B \frac{dc_B}{c}(\omega) + X_{ij}^C \frac{dc_C}{c}(\omega) + X_{ij}^P \frac{dc_P}{c}(\omega) + X_{ij}^Q \frac{dc_Q}{c}(\omega) + X_{ij}^S \frac{dc_S}{c}(\omega),$$ (1)

where X_{ij}^n is the fraction of the total path length through each region n, as indicated by the superscript. The value on the left-hand side of equation (1) is the measured path-averaged phase-velocity anomaly, which is expressed with respect to phase velocity in PREM [*Dziewonski and Anderson*, 1981]. This pure-path inversion yields values of phase-velocity anomaly for six regions at each frequency; phase-velocity anomalies are converted into absolute phase velocities using the PREM phase velocities as reference. We use the values determined for region S (Precambrian cratons) as the center of the observed phase-velocity range. Table 1 summarizes the number of measurements used and the phase velocity determined for region S from the pure-path inversion. Supporting information Figure S1c shows the path coverage for 100 s Rayleigh wave global data set.

In supporting information Figure S1, we compare the cratonic regions in GTR1 and CRUST1.0 [*Laske et al.*, 2013]. There is considerable overlap between the two, although they are not in perfect agreement. To investigate to what extent the choice of regionalization affects our results, we have re-calculated the center (pure-path) phase velocities using the CRUST1.0 regionalization instead of GTR1. The two sets of cratonic phase-velocity values are nearly identical. At periods of 40 and 43 s the difference is approximately 0.01 km/s (0.25%), and at all other periods the difference is <0.005 km/s. Thus, the choice of regionalization has a negligible impact on our results and conclusions.

The width of the phase-velocity range that characterizes cratons is obtained by considering only Rayleigh wave propagation paths with significant length through cratons. We identify measurements for which >60% of their total path length is through region S (Precambrian cratons) and calculate the mean and standard deviation of these phase-velocity measurements. The width of the cratonic phase-velocity range at each period is defined as twice the standard deviation at that period. In other words, the total range is the center phase velocity determined from the pure-path inversion of the global data set plus or minus one standard deviation determined from measurements with >60% of path length through cratons (Table 1).

There is a trade-off between required fraction of path length through cratons and the number of measurements that meet that criterion. Requiring a larger fraction results in fewer measurements, whereas allowing a smaller fraction includes observations with less sensitivity to cratonic structure. Figure 2a shows that when the criterion of total path length through craton is increased to 65, 70, or 75%, the number of measurements available becomes too small to be useful, especially at long periods. While the mean phase velocity increases as the path length criterion increases (Figure 2b), reflecting the higher velocity that characterizes paths that are nearly exclusively cratonic, the standard deviation is less sensitive to the path length criterion (Figure 2c). Only when the path length criterion is very restrictive (70–75%) does the standard deviation vary considerably from the value determined for a path length criterion of 60%, as a result of the small data sets that meet these criteria. We note that the mean phase velocities approach but never exceed the pure-path velocity that defines the middle of our range, suggesting that it is a reasonable value for paths that are exclusively cratonic and supporting our choice to use this value as the center. The low-velocity end of our range approximately coincides with the mean phase velocity determined using a path length criterion of >60% (Figure 2b).

When cratons are defined using CRUST1.0 (supporting information Figure S1), the standard deviation determined from measurements with >60% of path length through cratons is smaller than when GTR1 is used. The CRUST1.0 regionalization allows a much larger number of paths through North America and Eurasia than GTR1 and a similar number through the other continents, resulting in values of the standard deviation that are, depending on period, 70–80% of those determined with GTR1.
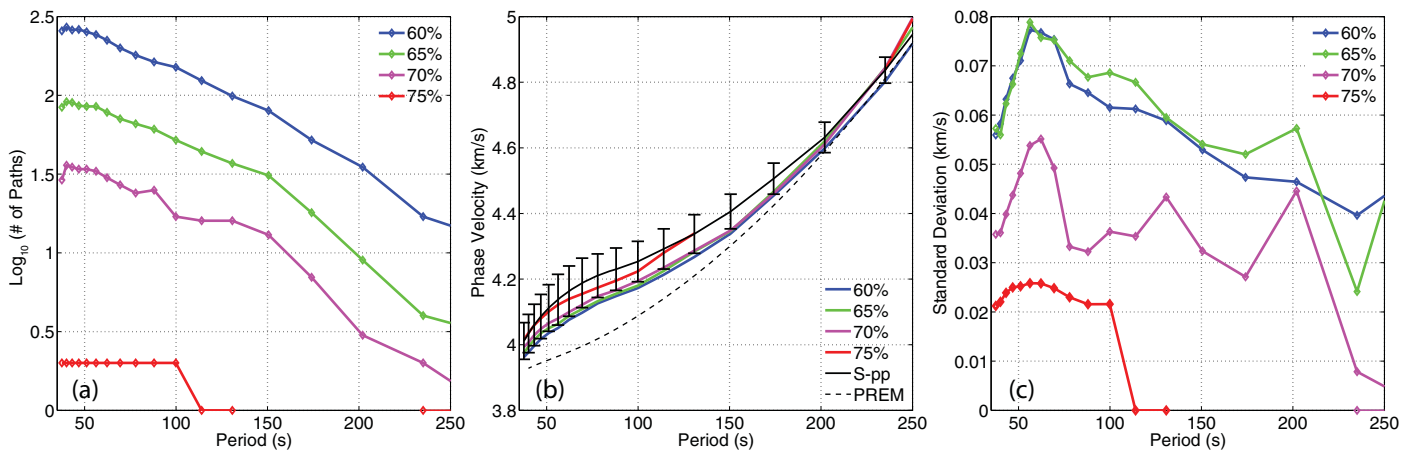
Figure 2. (a) Impact on the number of qualifying paths of the criterion governing allowable fraction of total path length through cratons. Including all paths with >60% of their length through region S in GTR1 [*Jordan*, 1981] permits 271 paths at 40 s and 17 paths at 235 s. Increasing the path length threshold value to 65, 70, and 75% results in fewer paths at all periods. Indeed, including only paths with >75% of their length through region S (red) permits at most two paths at short periods and as few as zero paths at longer periods. (b) Rayleigh wave phase-velocity curves. Solid black curve (S-pp) shows the value obtained from pure-path inversion of the global data set for phase velocity in six tectonic regions; the result for region S is plotted here. Colored curves show the mean phase velocity calculated from the subset of the global data set that meets the criterion allowable fraction of total path length through cratons. Mean phase velocities obtained using path length threshold values of 60, 65, 70, and 75% are plotted. Error bars on S-pp show ±one standard deviation of the observations that meet the 60% threshold. Rayleigh wave phase velocity for PREM is shown for comparison. (c) Standard deviation of the observations that meet the 60, 65, 70, and 75% path length threshold.

Figure 3a summarizes the geographic distribution of Rayleigh wave paths (period = 51 s) for which >60% of their total length is through region S. Of the 253 paths plotted, 168 sample the North American craton, 18 sample the South American craton, 54 sample the cratons in Africa, and 13 sample cratons in Western Australia. Figure 3b compares the mean cratonic phase velocity from each continent, calculated from these paths, to our global range. With the exception of Africa, the mean velocities for different regions are very similar. Inclusion of the African paths in our global data set results in a larger standard deviation than would otherwise be the case, and thus our global cratonic phase-velocity range is not likely to be too narrow and, in fact, may be too broad. Lower phase velocities are characteristic of the cratonic regions in Africa, as has been noted by others [e.g., *Weeraratne et al.*, 2003; *Pedersen et al.*, 2009], which may have the effect of slightly reducing our pure-path velocities relative to a regionalization scheme that excludes Africa.
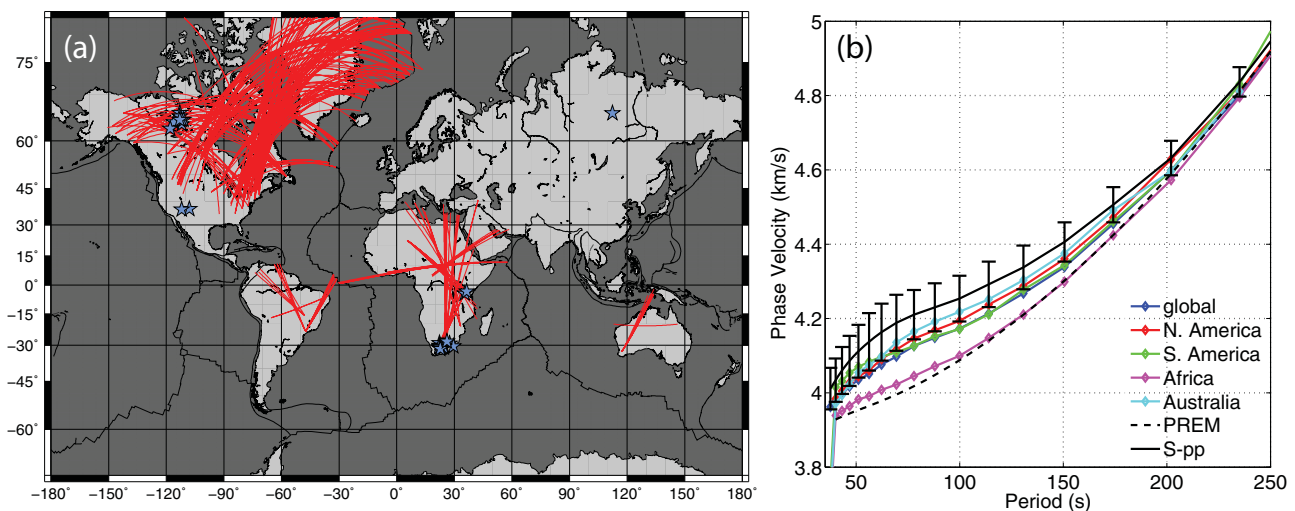
Figure 3. (a) Geographic distribution of 253 paths that meet the 60% path length threshold for 51 s Rayleigh waves. Stars show the locations of mantle xenoliths from Figure 4a. These paths are used only to obtain estimates of standard deviation; the pure-path phase velocities are obtained from a global data (Table 1 and supporting information Figure S1). (b) Rayleigh wave phase velocity. Solid black curve with error bars and dashed curve are as in Figure 2b. Colored curves show mean values of observations that meet the 60% path length threshold for four different cratonic regions.

3. Methods

One-dimensional Earth models are generated, and frequency-dependent phase velocity is predicted for each Earth model to enable comparison to the global phase-velocity range described in the previous section. An Earth model is considered to be consistent with the observations if, at each of the 16 discrete periods between 40 and 235 s, its phase velocity falls within the global range. If phase velocity falls outside the global range at one or more periods, the Earth model is eliminated. Although this criterion for identifying acceptable models is consistent with earlier studies [e.g., *Lebedev et al.*, 2009; *Pedersen et al.*, 2009], in the supplemental material we describe the results obtained if a different criterion, based on the chi-squared misfit between observed and predicted phase velocity, is used. We generate 1-D Earth models using two approaches. The first approach incorporates constraints on the temperature structure of the cratonic upper mantle; these 1-D profiles of temperature are converted into shear velocity, using several scaling relations, to generate 1-D Earth models that permit comparison to the Rayleigh wave observations. The second approach uses randomly generated profiles of shear velocity with depth. There are merits to both approaches. The second approach frees us from the constraints imposed by an assumed thermal structure and temperature-velocity scaling, while the first approach recognizes that several data sets, including xenolith thermobarometry [e.g., *Lee et al.*, 2011] and surface heat flow [e.g., *Rudnick et al.*, 1998], provide independent and useful information about upper mantle thermal structure.

3.1. Geotherm-Generated Earth Models

To calculate profiles of temperature with depth $T(z)$, we consider solutions to the equation of 1-D steady state heat conduction with volumetric heat production

$$k\frac{d^2T}{dz^2} = -\rho H, \tag{2}$$

where H is the heat generation per unit mass, ρ is density, and k indicates thermal conductivity. For a layer of thickness Δz with temperature T_t and heat flow q_t specified at the top of the layer, the temperature T_b and heat flow q_b at the base of the layer are given by

$$T_b = T_t + \frac{q_t}{k}\Delta z - \frac{\rho H}{2k}(\Delta z)^2, \tag{3}$$

$$q_b = q_t - \rho H \Delta z. \tag{4}$$

Heat flow and temperature at the top of the first layer ($z = 0$) are prescribed; we test seven values of surface heat flow (25, 30, 35, 40, 45, 50, and 55 mW/m^2) [e.g., *Nyblade and Pollack*, 1993; *Shapiro and Ritzwoller*, 2004] and fix surface temperature to 0°C. Temperature and heat flow are determined from the surface to 400 km depth, using 2000 layers of thickness = 200 m; the profile was then resampled to 80 layers of thickness = 5 km. Different values of radiogenic heat production are assigned to the upper crust, lower crust, and mantle lithosphere. To allow for different contributions of crustal heat production to the surface heat flow, we test several different values of heat production for each layer, using five combinations of heat-production values (Table 2) and five values of crustal thickness (30, 35, 40, 45, and 50 km). The range of crustal properties tested is informed by the range of values suggested by the literature [e.g., *Nyblade and Pollack*, 1993; *Rudnick and Fountain*, 1995; *Rudnick et al.*, 1998; *Rudnick and Nyblade*, 1999; *Shapiro and Ritzwoller*, 2004; *Mareschal and Jaupart*, 2013]. The thickness of the upper crust is fixed at 10 km for all scenarios. The bulk crustal heat production, calculated as

$$\frac{(\rho H)_{UC} \times 10 + (\rho H)_{LC} \times (d - 10)}{d}, \tag{5}$$

where d is total crustal thickness in km and the subscripts UC and LC indicate upper and lower crust, respectively, ranges from 0.3 to 0.9 (Table 2). Thermal conductivity k is constant within the crust (Table 2) and varies with temperature T in the mantle [*Jaupart and Mareschal*, 1999]

$$k(T) = \frac{1}{0.174 + 0.000265T} + (3.68 \times 10^{-10})T^3. \tag{6}$$

Geotherms are required to intersect the mantle adiabat at depth. Adiabatic temperature is calculated using

Table 2. Summary of the Parameter Values Utilized to Generate Cratonic Temperature Profiles[a]

	1	2	3	4	5
UC heat production (μW m^{-3})	0.5	0.5	0.5	0.6	1.8
LC heat production (μW m^{-3})	0.25	1.00	0.25	0.60	0.25
Mantle heat production (μW m^{-3})	0.01	0.01	0.01	0.02	0.01
Thermal conductivity (Wm^{-1} K^{-1})	2.5	2.6	2.7	2.6	2.5
Bulk crustal heat production (μW m^{-3})			0.3–0.9		
Surface heat flow (mW m^{-2})			25, 30, 35, 40, 45, 50, 55		
Mantle potential temperature ($^\circ$C)			1275:25:1500		
Crustal thickness (km)			30, 35, 40, 45, 50		

[a]Five sets of radiogenic heat-production values are considered, and UC and LC refer to the upper and lower crust, respectively.

$$T_{ad}(z) = T_P \left(1 + \frac{\alpha g z}{c_p} \right), \tag{7}$$

where T_P is mantle potential temperature, g is the acceleration due to gravity, α is the coefficient of thermal expansion (2.9×10^{-5} K^{-1}), and c_p is the specific heat at constant pressure (1350 J kg^{-1} K^{-1}). We consider 10 values of T_P (1275, 1300, 1325, 1350, . . ., 1500°C); these potential temperatures span the range inferred beneath the global mid-ocean ridge system [*Dalton et al.*, 2014] and overlap with the values commonly utilized in studies of the cratonic upper mantle [e.g., *Rudnick et al.*, 1998; *Jaupart and Mareschal*, 1999; *Carlson et al.*, 2005]. The adiabatic temperature gradient with depth thus ranges between 0.27 and 0.32°C/km.

In total 1750 geotherms are generated. Figure 4a compares the a priori distribution of geotherms to pressure-temperature constraints on upper mantle temperature obtained from xenolith thermobarometry [*Lee et al.*, 2011]. The range of geotherms tested in this study overlaps with the xenolith constraints and also includes hotter and colder scenarios. We have chosen to test a broad range of geotherms and allow the phase-velocity constraints to guide the selection of acceptable models. For a given value of surface heat flow, the variations in T_P and bulk crustal heat production result in a distribution of geotherms, with lower temperatures corresponding to high crustal heat production and a deeper intersection with the adiabat for higher T_P values.

We use the parameterization of *Jackson and Faul* [2010] to convert the temperature profiles into profiles of vertically polarized shear velocity (V_{SV}). This parameterization is based on laboratory experiments performed on forsterite-90 olivine and includes both elastic and anelastic effects on shear velocity. Since the anelastic properties of mantle rocks are not as well constrained as the elastic properties, we test a range of anelastic parameters by varying grain size (1, 50, and 100 mm) and period (1, 25, 50, 100, and 200 s). In the parameterization of *Jackson and Faul* [2010], shear velocity is positively correlated with grain size and negatively correlated with period; however, the dependence of shear velocity on grain size and period is minimal at temperatures <900°C. This yields 15 separate temperature-velocity scaling relations, applied to depths <400 km, for each temperature profile, yielding a total of 26,250 geotherm-generated 1-D Earth models. At depths >400 km, all parameters in the Earth models are fixed to their values in PREM. The general shape of each velocity profile is determined by the general shape of the temperature profile, and the magnitude of wave speed is controlled by the details of the temperature-velocity scaling. As a consequence of using 15 temperature-velocity scalings for each temperature profile, we will not be able to uniquely identify a temperature profile that is most compatible with the Rayleigh wave observations. However, as shown in section 4, we can use our results to place bounds on the range of parameters (i.e., mantle potential temperature, surface heat flow, and crustal heat production) that are compatible with the observations. By testing a range of temperature profiles and scaling relations, our model-space search considers a wide variety of velocity structures whose shape and magnitude are broadly consistent with xenolith and surface heat flow constraints on temperatures in the continental upper mantle.

For each 1-D Earth model, it is necessary to specify not only V_{SV} but also horizontally polarized shear velocity (V_{SH}), the speed of vertically and horizontally propagating P waves (V_{PV} and V_{PH}), density, shear and bulk attenuation (Q_μ^{-1} and Q_κ^{-1}), and the anisotropic parameter η. We calculate V_{SH} by fixing the difference V_{SH}-V_{SV} to its value in PREM, and V_{PH} and V_{PV} are obtained using the constant scaling factor 1.85: $V_{PH} = 1.85V_{SH}$ and $V_{PV} = 1.85V_{SV}$. Values of density, attenuation, and η are fixed to their values in PREM. All geotherm-generated Earth models contain a 37 km thick crust; this thickness as well as the elastic properties and
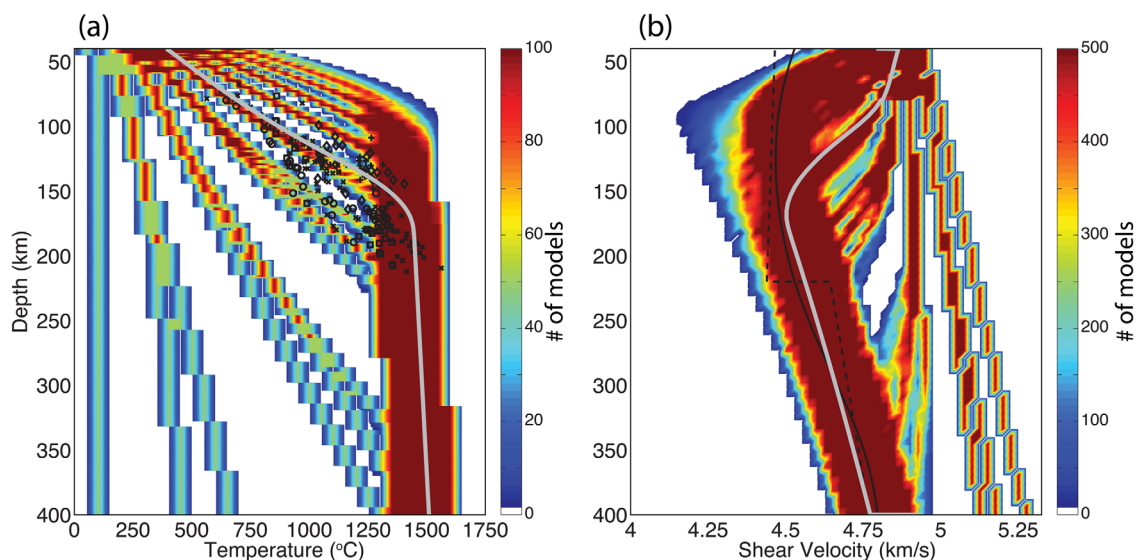
Figure 4. (a) A priori distribution of 1750 geotherm profiles considered. Black symbols show pressure-temperature constraints from cratonic mantle xenoliths [*Lee et al.*, 2011]. Thick gray curve shows the average temperature profile of the 165 acceptable Earth models. Xenoliths are shown for the Slave craton (circles), Tanzania (diamonds), South Africa (x), Siberia (squares), and the Colorado Plateau (+). (b) A priori distribution of Voigt-averaged isotropic shear velocity ($[2*V_{SV} + V_{SH}]/3$) for 26,250 Earth models generated by scaling the temperature profiles in Figure 4a. Thick gray curve shows the average V_S profile of the 165 acceptable Earth models.

density of the crust are obtained from CRUST2.0 [*Bassin et al.*, 2000], using the values that apply to Archean crust with no sediments. Figure 4b summarizes the a priori distribution of geotherm-generated velocity profiles tested. Sensitivity of our results to assumptions about the V_P/V_S ratio and crustal thickness are discussed in section 6.
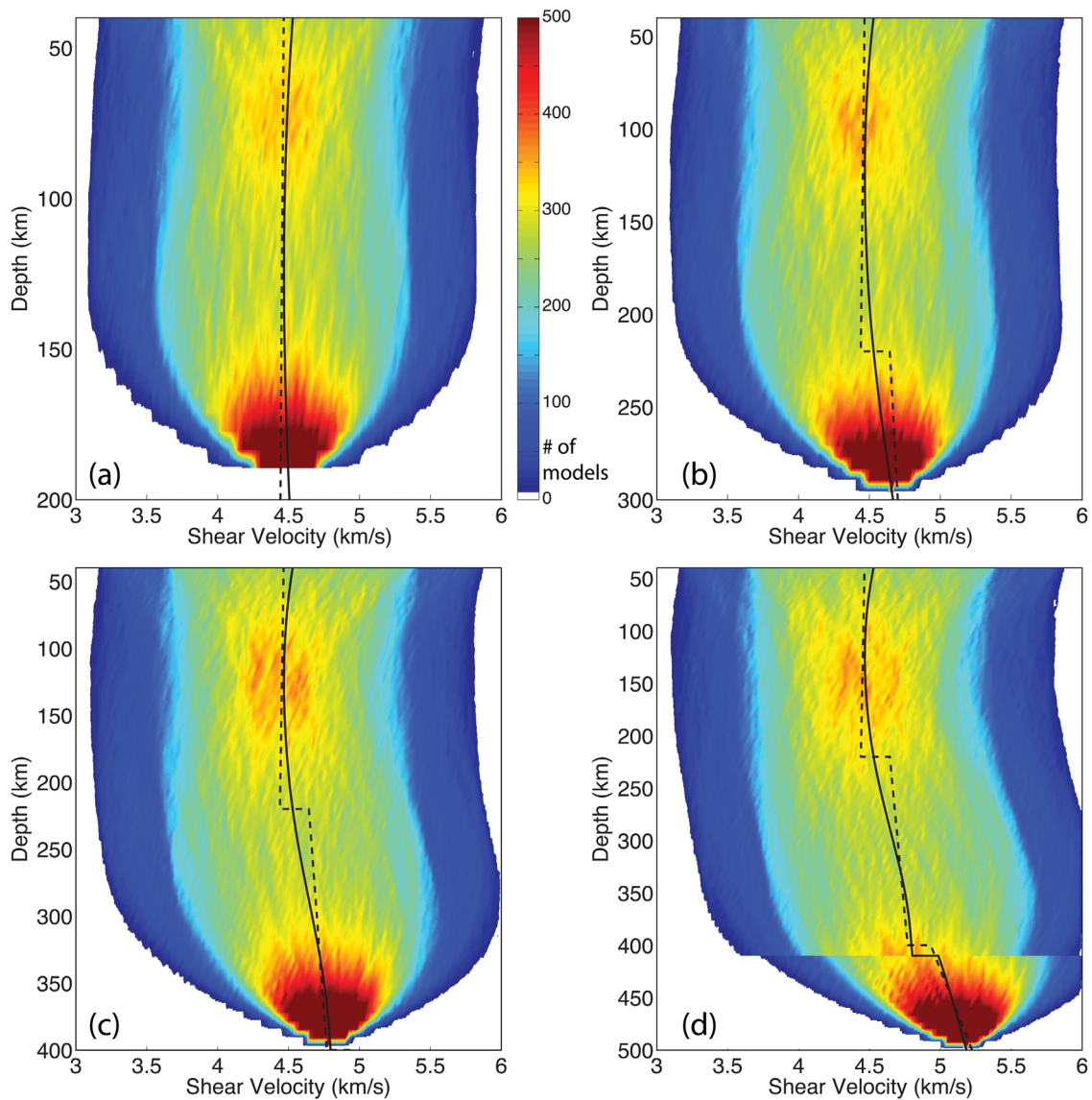
3.2. Randomly Generated Earth Models

For the randomly generated Earth models, the global 1-D Earth model STW105 [*Kustowski et al.*, 2008] is used as the reference model with respect to which the perturbations are calculated. A total of 80,000 1-D models are evaluated; all models contain the same 37 km thick Archean crust that is also used for the geotherm-generated models. For 20,000 models, the perturbations are confined to the depth range 37–200 km; all parameter values at depths >200 km are fixed to their values in STW105. A separate set of 20,000 models is generated for which the perturbations are confined to a slightly broader depth range, 37–300 km. Two additional sets of 20,000 models each contain perturbations restricted to depth ranges 37–400 and 37–500 km, respectively. With these four sets of models, which we refer to as "depth-range scenarios," we can explore how the resulting phase-velocity values associated with cratons depend on the depth range over which elastic properties are allowed to deviate from the average global value.

The decision about how to parameterize the random perturbations is obviously a subjective one. The broad depth-sensitivity kernels of Rayleigh waves allow numerous velocity profiles, including those containing discontinuities and localized perturbations, to produce very similar phase-velocity curves. Here we focus on smooth perturbations, similar to those described by tomographic models constrained by surface waves, and parameterize the perturbations to STW105 as a function of depth using a quartic function (degree-4 polynomial):

$$\frac{\delta v}{v} = A + By + Cy^2 + Dy^3 + Ey^4, \tag{8}$$

where A, B, C, D, and E are randomly generated coefficients and y is depth normalized by the maximum depth in the interval of interest. For example, for models containing perturbations in the depth range 37–300 km, $y = 0.123$, and $y = 1.000$ at the top and bottom of the depth interval, respectively. To obtain a 1-D model, a trial model is first calculated by randomly generating the five coefficients, which have values in the range −1 to +1. For the results described here, $\delta v/v = 0$ at $y = 1$ (i.e., the 1-D model is forced to return to STW105 at the bottom of the prescribed depth range), which in practice is accomplished by calculating the value of A that satisfies this criterion. Thus, for these models, A is not randomly generated. If the

Figure 5. A priori distribution of Voigt-averaged isotropic shear velocity for the randomly generated models. Perturbations to 1-D reference model STW105 are permitted in the depth range (a) 37–200 km; (b) 37–300 km; (c) 37–400 km; and (d) 37–500 km. Note the different vertical axes in each figure. Dashed and solid black lines show isotropic shear velocity from PREM and STW105, respectively.

absolute value of $\delta v/v$ exceeds 20% (or 30% for certain scenarios) at any point in the prescribed depth range, the trial model is discarded and the program generates a new set of coefficient values. This process is repeated until an acceptable trial model can be found. For each of the four depth-range scenarios considered, we have generated 10,000 models with limits $-0.2 \leq \delta v/v \leq 0.2$ and 10,000 models with limits $-0.3 \leq \delta v/v \leq 0.3$ in order to sample broadly while also avoiding highly unrealistic Earth models. The value of $\delta v/v$ is converted to absolute velocity and assigned to V_{SV}; V_{SH} is calculated for each Earth model by preserving the difference V_{SH}-V_{SV} that is contained in STW105. We also preserve the ratios V_{PV}/V_{SV} and V_{PH}/V_{SH} that are contained in STW105 and calculate V_{PV} and V_{PH} accordingly. All other parameters are unchanged from their values in STW105. Figure 5 summarizes the a priori distribution of randomly generated velocity profiles tested and shows that while our sampling strategy casts a wide net in an effort to be inclusive, most of the shear-velocity values tested are within approximately 10% of the average global value. The convergence of all models back to STW105 at the base of each depth range is apparent in the very high density of the a priori distributions at the bottom of each panel in Figure 5.
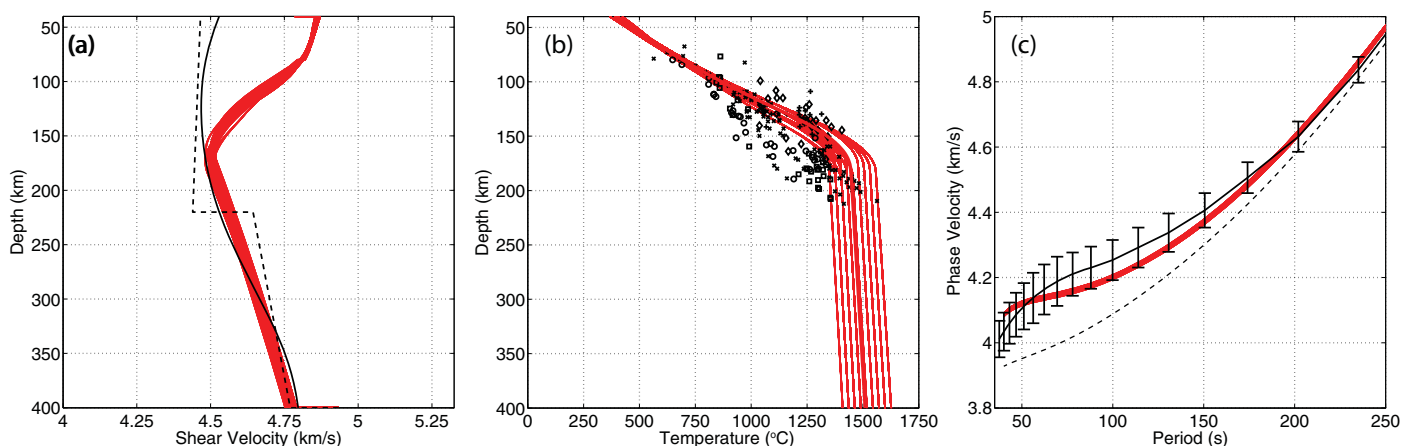
Figure 6. (a) Voigt-averaged shear-velocity profiles for the 165 geotherm-generated models that provide an acceptable fit to the observations. Dashed and solid black curves show PREM and STW105. (b) Temperature profiles corresponding to the shear-velocity profiles in Figure 6a. Symbols as in Figure 4a. (c) Phase-velocity curves corresponding to the shear-velocity profiles in Figure 6a. The observed range and the PREM phase velocity (dashed) are plotted for comparison.

4. Results for Geotherm-Generated Earth Models

Of the 26,250 geotherm-generated models tested, 165 yield Rayleigh wave phase-velocity values that fall within the observed range for cratons at all periods between 40 and 235 s. Figure 6a shows the isotropic shear velocity (Voigt average; $V_S = [2*V_{SV} + V_{SH}]/3$) from these acceptable Earth models, and Figure 6b shows the corresponding temperature profiles. Figure 6c compares the predicted phase velocity to the observed range. The acceptable temperature profiles show a larger spread of values than would be expected from the narrow range of the shear-velocity profiles. This is a consequence of using several different temperature-velocity scaling relationships; as a result, there is not a unique velocity profile for each temperature profile.

Of the 165 acceptable models, 110 correspond to geotherms generated with surface heat flow = 30 mW/m^2, and 60 of these 110 models have mantle potential temperature values in the range 1425–1475°C (supporting information Figure S2). No models with surface heat flow = 25 mW/m^2 can fit the observations. Supporting information Figure S3a shows that phase-velocity curves corresponding to models with surface heat flow = 25 mW/m^2 are too high at periods <90 s; supporting information Figure S3b shows that with 35 exceptions, models with surface heat flow = 35 mW/m^2 predict phase velocity that is either too low at intermediate periods or too high at short periods. Of the 165 acceptable models, 110 have bulk crustal heat production in the range 0.3–0.4 μW m^{-3} (supporting information Figure S2). All of the acceptable models contain a low-velocity zone. The velocity minimum within the LVZ is approximately 4.5 km/s for the acceptable models. The depth of the LVZ shows little variation; depth to the velocity minimum varies from 157.8 to 178.8 km, even though a much wider range of values was tested (supporting information Figure S4).

While the 165 acceptable models have Rayleigh wave phase velocity that falls within the observed range and therefore meets our criterion, Figure 6c makes clear that the shape of these predicted dispersion curves is different than the shape of the center of the observed range. Predicted phase velocity is higher at periods <50 s and lower at periods 60–150 s than the observed center, resulting in a predicted phase-velocity curve that is nearly flat from 40 to 100 s. This fundamental difference in shape makes the geotherm-generated models very sensitive to the width of the observed range; limiting even slightly the width of the observed range would cause nearly all of these acceptable models to be rejected. For these Earth models, reducing the shear velocity in the shallowest mantle and increasing the shear velocity beneath it would lead to better agreement with the observations and less sensitivity to the width of the observed range.

5. Results for Randomly Generated Earth Models

The a posteriori distribution of randomly generated Earth models is summarized in Figure 7, and the corresponding phase-velocity curves are compared to the observations in Figure 8. For Earth models for which the random perturbations are confined to the depth range 37–200 km, we identify 695 acceptable models
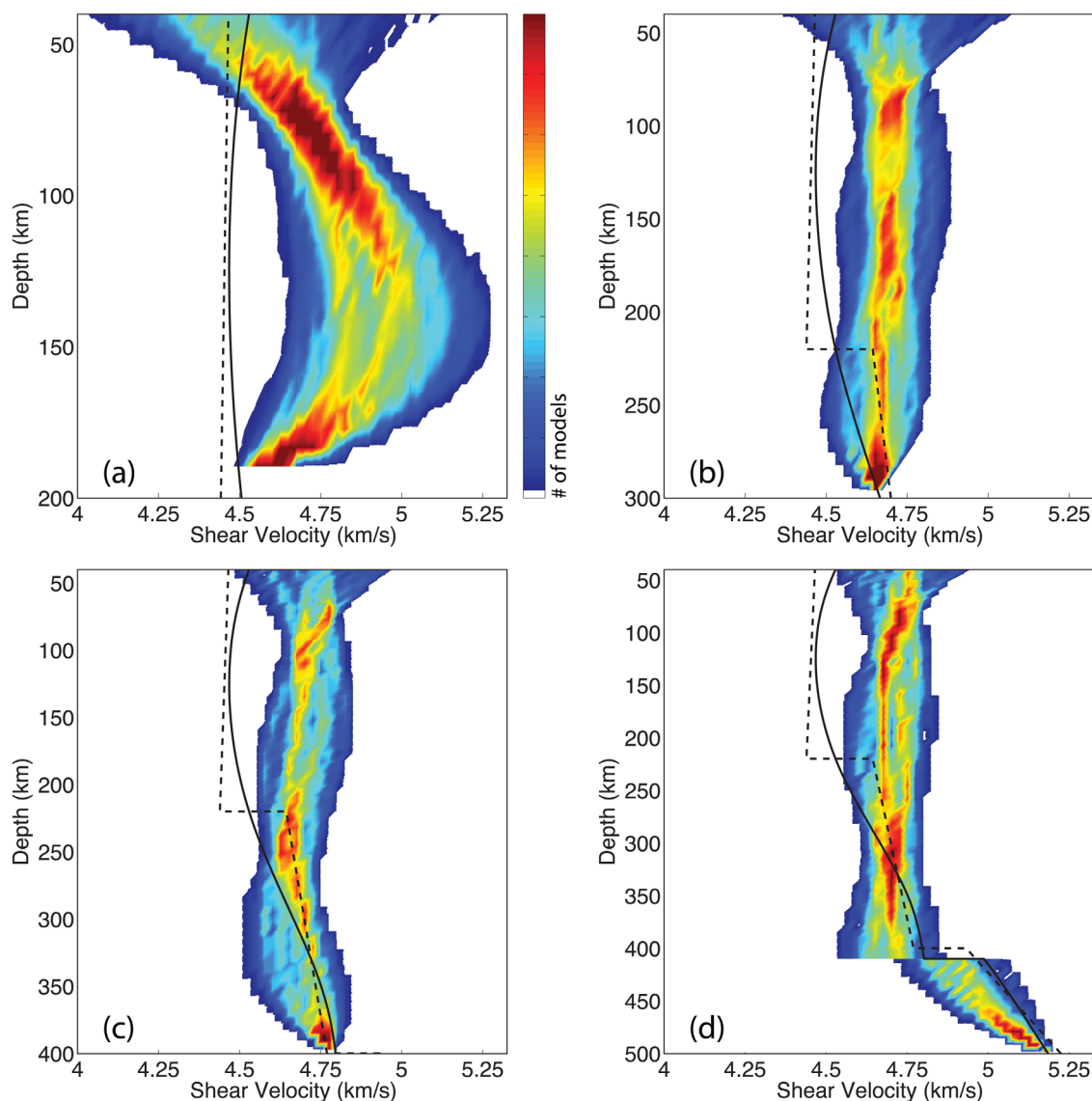
Figure 7. Distribution of Voigt-averaged shear velocity for the a posteriori randomly generated Earth models. (a) Summary of the 695 models for which the perturbations are confined to the depth range 37–200 km. Color-scale range is 0–80. (b) 175 models for which perturbations are confined to 37–300 km; color-scale range is 0–40. (c) 67 models for which the perturbations are confined to 37–400 km; color-scale range is 0–20. (d) 57 models for which the perturbations are confined to 37–500 km; color-scale range is 0–15. Solid and dashed black curves show isotropic shear velocity from STW105 and PREM.

from the comparison of observed and predicted phase velocity. This number is reduced to 175, 67, and 57 when perturbations are confined to the depth ranges 37–300, 37–400, and 37–500 km, respectively. In general the predicted phase-velocity curves for the acceptable randomly-generated models more closely match the shape of the observed range than the predicted curves corresponding to the geotherm-generated models (Figure 6c). The curves for the geotherm-generated models are flat at periods <100 s, whereas the center of the observed range is characterized by a steep increase in phase velocity at these periods.

It is clear that the a posteriori randomly generated models exhibit higher shear velocity than STW105 and PREM [*Dziewonski and Anderson*, 1981]. The maximum depth extent of the elevated velocity varies somewhat from model to model and depends on the depth range to which the perturbations are confined. We note that since our observations are determined from fundamental-mode Rayleigh waves at periods <240 s, our analysis has limited sensitivity at depths >400 km. Figure 9a compares the "average" isotropic shear velocity from each of the four depth-range scenarios considered. To calculate these average profiles, at each depth the V_S value corresponding to the maximum density in the a posteriori distribution is
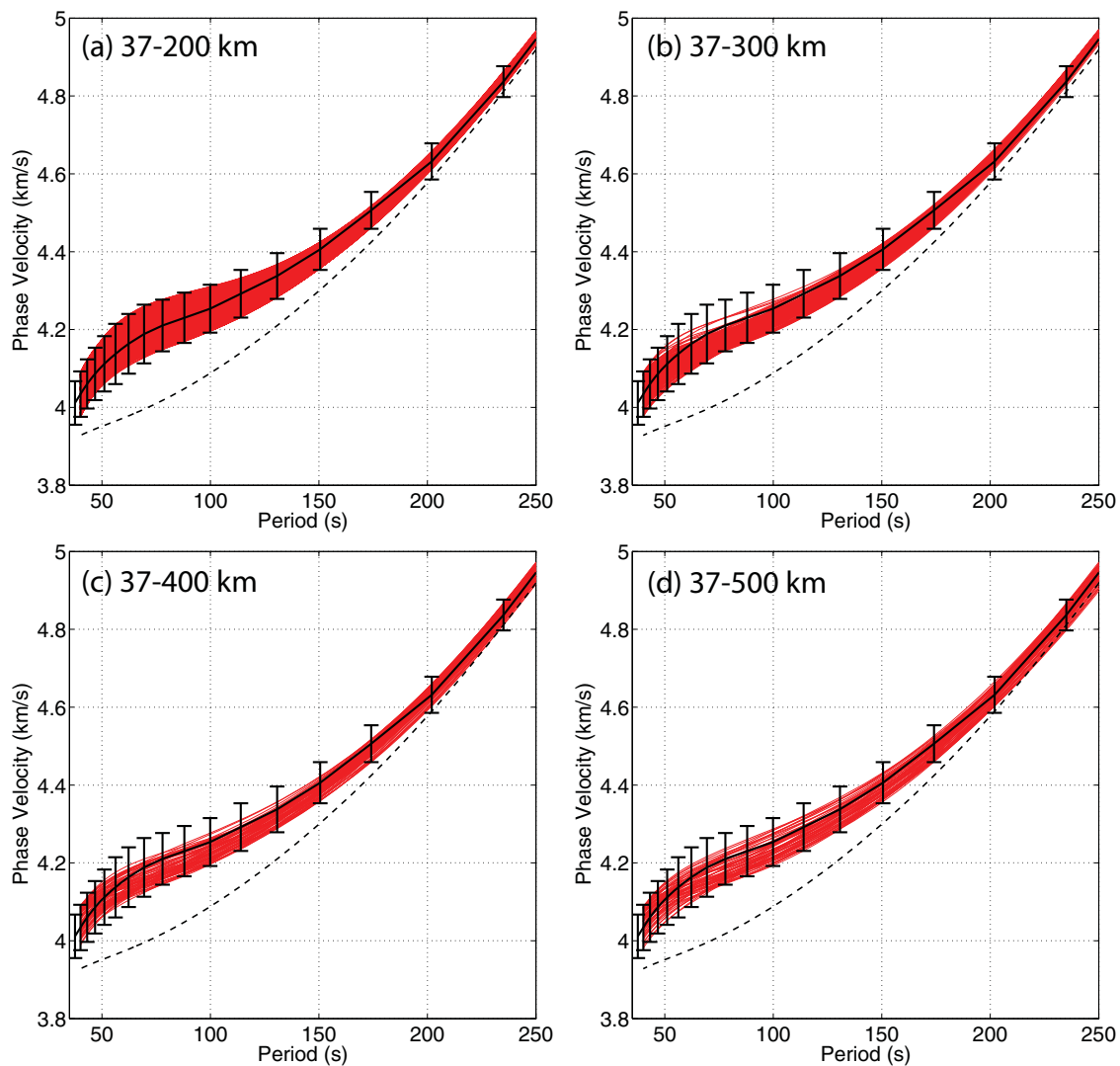
Figure 8. Rayleigh wave phase-velocity curves for the a posteriori randomly generated models. The observed range (solid black) and PREM phase velocity (dashed black) are plotted for comparison. Results obtained for the four depth-range scenarios are shown separately.

identified; if two V_S values have the same maximum density, their values are averaged. Very high wave speed is associated with the acceptable models that have perturbations confined to 37–200 km. Since those models are forced back to STW105 values (i.e., global average) at depths >200 km, high velocities are needed at shallow depths to compensate for the average velocities at greater depth.

Average shear-velocity profiles for the other depth-range scenarios are similar to each other, lower than the 37–200 km scenario, and higher than the global average (STW105) to approximately 300 km depth. When a narrower range of observed phase velocity is used to select the acceptable randomly generated models (±0.5 SD instead of ±1.0 SD), the average shear velocity is approximately 0.05 km/s higher (Figure 9b) for all depth-range scenarios to 200–250 km. Figure 9c demonstrates good agreement in shape and magnitude between regional seismic studies from cratons (Figure 1) and the average velocity profiles from the randomly generated models. The shape of the average geotherm-generated models, on the other hand, has little in common with the observed models.

We are interested not only in the magnitude of shear velocity but also in the gradient of shear velocity with depth, which provides useful information about thermal and chemical gradients with depth and, potentially, bottom of the lithosphere. When the perturbations are confined to depths <200 km, 92% of the acceptable models are characterized by a positive velocity gradient with depth in the depth range
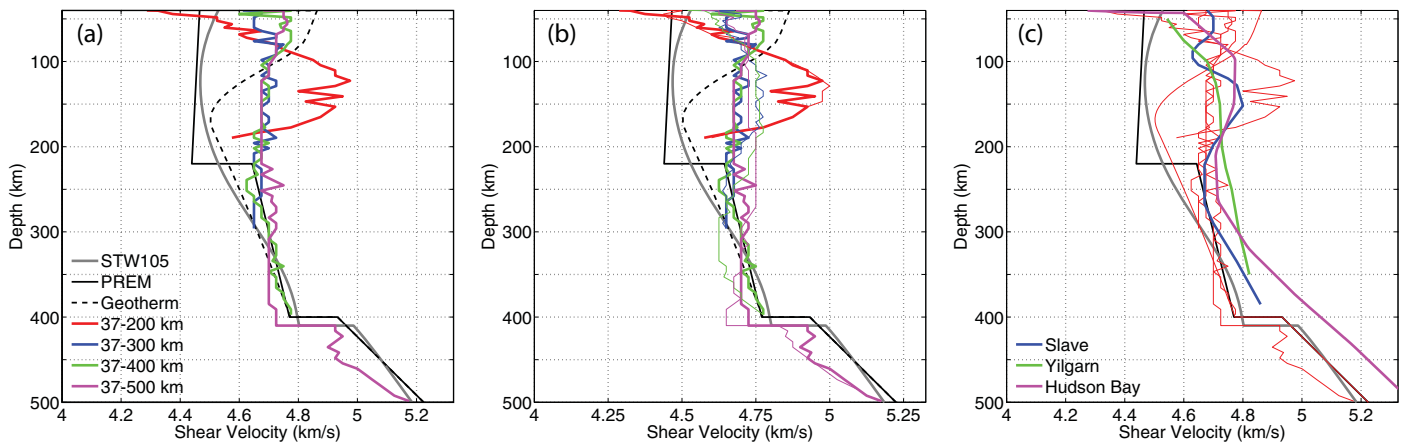
Figure 9. (a) Voigt-averaged shear velocity for the a posteriori randomly generated models. Black dashed curve shows the average geotherm-generated model (Figure 4b). Colored curves show velocity corresponding to the maximum in the 2-D histograms (i.e., Figure 7). PREM and STW105 are plotted for comparison. (b) Same as in Figure 9a, with thin colored lines corresponding to average shear velocity of the randomly generated models obtained when the observed phase-velocity range is only ±0.5 SD instead of ±1.0 SD. (c) Models from Figure 9a, shown with thin red lines, compared to observed shear-velocity profiles from the Slave craton, Yilgarn, and Hudson Bay (i.e., Figure 1).

50–100 km, with an average gradient of 5.9×10^{-3} km s^{-1}/km. The first and third quartiles are 3.1×10^{-3} and 9.0×10^{-3} km s^{-1}/km. (For reference, we can contrast these values with the average velocity gradient in the depth range 50–100 km for the acceptable geotherm-generated models, which is -2.3×10^{-3} km s^{-1}/km.) However, when the random perturbations are allowed to extend to 300, 400, or 500 km, the percentage of acceptable models with a positive velocity gradient at shallow depths is much smaller—54, 49, and 49%, respectively—as are the values of the average velocity gradient: 1.91×10^{-4} km s^{-1}/km, 7.00×10^{-6} km s^{-1}/km, and -1.85×10^{-4} km s^{-1}/km. Examination of the first and third quartiles (-1.35×10^{-3}/ 1.99×10^{-3}, -1.32×10^{-3}/1.30×10^{-3}, and -1.23×10^{-3}/0.93×10^{-3} km s^{-1}/km for the 300, 400, and 500 km depth-range scenarios, respectively) reveals that the shallow-level gradients are neither strongly negative nor strongly positive. Rather, the values of velocity gradient are roughly evenly distributed about zero with magnitudes that are much smaller than for the acceptable models of either the 200 km depth-range scenario or the geotherm-generated models.

We use cluster analysis to classify the acceptable randomly generated models by shape, following the approach applied by *Lekic and Romanowicz* [2011b] to global shear-velocity models. Profiles of isotropic shear velocity are extracted from all acceptable Earth models, and a k-means clustering scheme is applied to those profiles. Clustering is performed using the correlation distance rather than the squared Euclidean distance, as we are primarily interested in the shape and not the amplitude of the velocity profiles for this exercise. For each depth-range scenario (37–200, 37–300, 37–400, and 37–500 km) we allow four clusters to form. We experimented with using between two and eight clusters and found that 3–4 groupings were needed for each depth-range scenario; for consistency we use four clusters for all scenarios.

Figure 10a shows the four profiles identified when cluster analysis is applied to the acceptable randomly generated models with perturbations confined to 37–200 km. Two of the profiles (groups 2 and 4) contain increasing shear velocity to ~120–150 km depth and do not contain a low-velocity zone. The other two profiles exhibit nearly constant velocity with depth; the group 1 profile contains a very slight LVZ at ~70 km. For the acceptable models with perturbations confined to 37–300 km, cluster analysis reveals four profiles with less variability than the four profiles in Figure 10a. Two profiles (groups 2 and 4) exhibit increasing velocity to 100–150 km (Figure 10b). Group 3 contains a slight LVZ at ~150 km while group 1 shows a positive velocity gradient with depth from 100 to 250 km. Similar results are obtained for the 37–400 and 37–500 km scenarios (Figures 10c and 10d): two of the clusters (groups 2 and 4) show increasing wave speed to ~150–200 km, one cluster (group 3) has a slight LVZ at ~200 km, and the fourth cluster has a small negative velocity gradient with depth to 300–400 km. Table 3 summarizes the number of individual profiles that belong to each cluster.

In the supporting information, we describe the results obtained if a selection criterion based on the chi-squared misfit between observed and predicted phase velocity is applied to the randomly generated
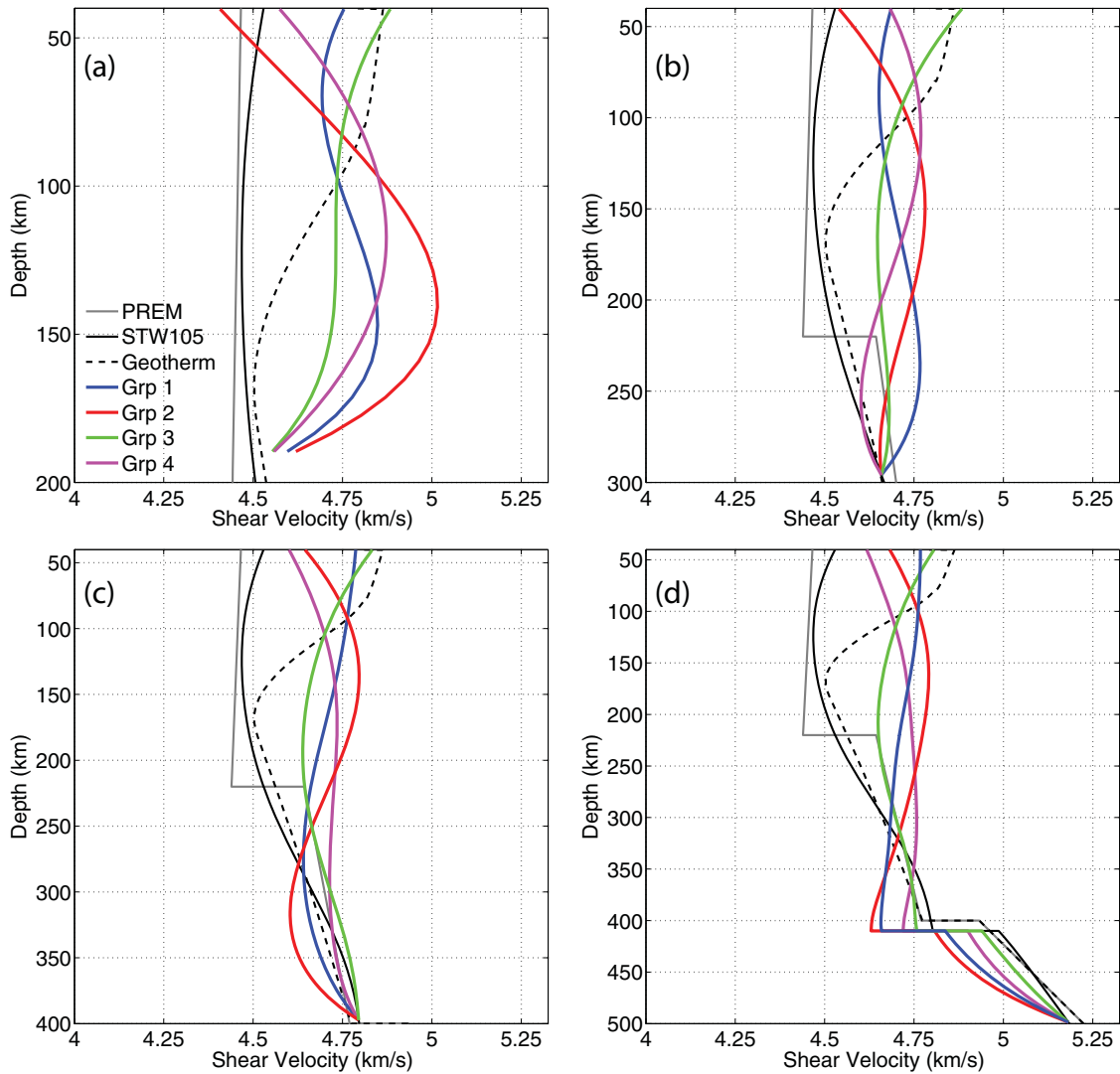
Figure 10. Result of applying k-means cluster analysis to the acceptable randomly generated models. (a) 37–200 km; (b) 37–300 km; (c) 37–400 km; and (d) 37–500 km. Each profile is an average of the individual profiles that belong to each cluster (Table 3). Shear velocity from PREM, STW105, and average of the acceptable geotherm-generated models are plotted for comparison. Note the different vertical axes.

models. Identifying acceptable models on the basis of the summed misfit over all periods instead of the requirement that predicted phase velocity falls within the observed range permits a larger number of acceptable models. Most of the successful Earth models identified with the misfit-based criterion but not the error-bar-based criterion depart from the range defined by the error-bar-based models for only a small portion of the total depth range. Using the misfit-based criterion does not identify, for example, an entirely new class of randomly generated Earth models that the error-bar-based criterion rejects. Instead, the misfit-based criterion results in only minor adjustments to the characteristics of the suite of successful Earth models.

Table 3. Number of Individual Profiles that Belong to Each Cluster Group for Each Depth-Range Scenario[a]

Depth Range (km)	Group 1 (Blue)	Group 2 (Red)	Group 3 (Green)	Group 4 (Magenta)
37–200	55 (8.0%)	491 (70.6%)	50 (7.2%)	99 (14.2%)
37–300	34 (19.4%)	42 (24.0%	50 (28.6%)	49 (28.0%)
37–400	16 (23.9%)	18 (26.9%)	22 (32.8%)	11 (16.4%)
37–500	13 (22.8%)	10 (17.5%)	23 (40.4%)	11 (19.3%)

[a]Values in parentheses indicate the percentage of the total number of models.

6. Discussion

In the sections below, we explore the effect on our results of several assumptions, and we investigate the implications of our results for the thermal structure of the cratonic lithosphere. Where the results from the randomly generated Earth models are utilized in this section, we focus on models with random perturbations confined to 37–400 km. We consider them representative of the 37–300 and 37–500 km results, based on the similarity of the a posteriori distributions for these three scenarios (Figure 7). We do not further explore results for the 37–200 km scenario, which, while intriguing, have little in common with observed shear-velocity profiles (e.g., Figure 9c).

6.1. Assumptions
6.1.1. V_P/V_S Ratio
For the randomly generated models, the V_P/V_S ratio in the mantle is set equal to the V_P/V_S ratio in the STW105 reference model. The V_P/V_S ratio of the randomly generated models therefore varies from 1.86 at 400 km to 1.80 at 200 km to 1.76 at 50 km; we refer to these values as the "default case" below. To test the sensitivity of the selection of acceptable models to this assumption, we modify the V_{PH} and V_{PV} values in a subset of our a priori randomly generated profiles, predict Rayleigh wave phase velocity for the modified models, and select acceptable models on the basis of comparison to the observed phase-velocity range. We focus on the 10,000 randomly generated models with random perturbations to STW105 between −30 and 30% confined to the depth range 37–400 km; we set $V_{PH}/V_{SH} = 1.85$ and $V_{PV}/V_{SV} = 1.85$ at all depths between 37 and 400 km for consistency with the geotherm-generated models. The primary effect of this change is slightly higher P wave speeds and higher Rayleigh wave phase velocity (by 0.01–0.02 km/s) at all periods relative to the default case; at all periods the magnitude of the phase-velocity change is smaller than the width of the observed phase-velocity range, which ranges from 0.08 km/s at 235 s to 0.15 km/s at 56 s. The average isotropic shear velocity of the acceptable models for this scenario is similar to the default case for depths <200 km and slightly lower for depths 200–400 km (supporting information Figures S5a and S5b). Isotropic shear velocity intersects and becomes slower than STW105 at ∼250 km depth, 50 km shallower than the default case.

For the geotherm-generated models, $V_P/V_S = 1.85$ for depths 37–400 km. *Afonso et al.* [2010] showed that V_P–V_S ratios calculated for cratonic mantle xenoliths fall in the range 1.77–1.80 for peridotites in the garnet stability field and 1.72–1.75 for peridotites in the spinel stability field. Since our assumed ratio of 1.85 is higher than these ranges, we recalculate V_{PH} and V_{PV} in all 26,250 geotherm-generated models using $V_P/V_S = 1.73$ for depths between 37 and 400 km. By comparing results obtained with $V_P/V_S = 1.73$ and $V_P/V_S = 1.85$, we are exploring the effects of two end-member values. The effect of this change on the Rayleigh wave phase velocity is slightly lower velocity, by approximately 0.02 km/s at 50 s (for comparison, width of observed range is 0.14 km/s) and 0.06 km/s at 200 s (width of observed range is 0.09 km/s), when $V_P/V_S = 1.73$ instead of $V_P/V_S = 1.85$. Using $V_P/V_S = 1.73$ permits a larger number of acceptable geotherm-generated models (1275 versus 165), and the average isotropic shear velocity of these models is higher by approximately 0.1 km/s at depths >150 km (supporting information Figure S6). These models have a low-velocity zone that is weaker than and in the same depth range as the acceptable models obtained with $V_P/V_S = 1.85$ ($V_P/V_S = 1.73$ also permits some models with a shallower low-velocity zone). These models also provide better agreement with the regional seismic profiles, although velocity is still slower than observed, than when $V_P/V_S = 1.85$. As is also the case when $V_P/V_S = 1.85$, the shape of the phase-velocity curves predicted for the acceptable models is flatter at periods <100 s than the observed range, and phase velocity at periods 60–125 s is lower than the center of the observed range for all acceptable models.

6.1.2. Crustal Thickness
The crustal properties assumed for the geotherm-generated and randomly generated models correspond to crustal type "G1: Archean, no seds" from CRUST2.0 [*Bassin et al.*, 2000]. Using the classification scheme of CRUST2.0, we have determined that G1 is the most common crustal type across all cratonic regions of the globe. We have also determined, using CRUST2.0, that the median crustal thickness for cratons is 39 km and that 80% of cratons have crustal thickness values between 33 and 43 km. To test the sensitivity of our results to the assumed crustal structure, we modify the crustal properties in a subset of our randomly generated profiles, predict Rayleigh wave phase velocity for the modified models, and select acceptable models on the basis of comparison to the observed phase-velocity range. As with the V_P/V_S sensitivity testing, we focus on the 10,000 randomly generated models with random perturbations to STW105 between −30 and

30% confined to the depth range 37–400 km. We replace the 37 km thick crust with a 45 km thick crust (crustal type "H2" in CRUST2.0); only 7% of cratons around the globe have crustal thickness >45 km [*Bassin et al.*, 2000].

The thicker crust reduces Rayleigh wave phase velocities at the shortest periods (<0.05 km/s at 50 s, which is a factor of 2–3 smaller than the observed phase-velocity range) and has little effect on phase velocity at intermediate and long periods. As a result, phase-velocity curves corresponding to the acceptable models can have slightly higher phase velocity at periods of 50–125 s than is the case with the 37 km crust. Figure 8c shows that with a 37 km crust, very few acceptable models have phase velocity higher than the center of the observed range at these periods, presumably because models with high phase velocity at 50–125 s have phase velocity at periods <50 s that exceeds the observed range. The thicker crust therefore allows a few additional models to fall within the observed range (50 models versus 23 models for a 37 km crust). The differences are minor, however, and the a posteriori distributions and the average isotropic shear-velocity profiles for the 37 and 45 km crust are nearly identical. We do not repeat this experiment for the geotherm-generated profiles, as the effect on phase velocity and on the distribution of the acceptable models would be very similar.

6.1.3. Quartic Polynomial

For the randomly generated profiles, the perturbations in shear velocity with respect to STW105 are prescribed using a degree-4 polynomial (equation (8)) that varies with normalized depth y such that the maximum value of y is 1.0 for each depth-range scenario. Using a normalized depth variable and a fixed-degree polynomial means that the randomly generated profiles will be smoother and less oscillatory in character for the 37–400 and 37–500 km scenarios than for the 37–200 and 37–300 km scenarios. We test whether the acceptable models for the 37–400 km scenario contain greater variability as a function of depth if the perturbations are prescribed using a degree-8 polynomial instead of a degree-4 polynomial. Using a degree-8 polynomial, we generate 10,000 models with random perturbations to STW105 between −30 and 30% confined to the depth range 37–400 km. Supporting information Figure S5c shows the distribution of acceptable models. Comparison with the acceptable models calculated with a degree-4 polynomial (supporting information Figure S5b) show that the use of a degree-8 polynomial allows velocity profiles that are more oscillatory as a function of depth, achieving higher wave speeds between 100 and 250 km and lower wave speeds at 300–400 km. The average shear-velocity profiles for the two scenarios, however, are very similar, with higher velocity than the global average to approximately 300 km depth.

6.1.4. Anisotropy

Mantle anisotropy may affect our analysis in two ways. Azimuthal anisotropy may affect the Rayleigh wave measurements from which our observed range is drawn. *Yuan and Romanowicz* [2010] showed azimuthal anisotropy of approximately 1–2% in the uppermost 400 km of the North American craton, and the global anisotropic phase-velocity maps of *Ekström* [2011] indicate a similar or perhaps smaller magnitude of azimuthal anisotropy in cratons. The center phase velocities of our observed range are determined by pure-path inversion of large global data sets with many crossing paths and thus should not be very susceptible to artifacts resulting from uneven azimuthal coverage. The width of our observed range is determined from a small number of Rayleigh waves traversing cratons, and it is apparent in Figure 3a that these paths do not provide even azimuthal coverage over the individual cratons. With a more even distribution of azimuths, it is possible that the distribution of observed phase velocities would be slightly broader, resulting in larger standard deviation values. However, given the small amount of azimuthal anisotropy observed in the cratonic upper mantle, this is a minor effect. Furthermore, the standard deviation values utilized in this study, which are likely to be overestimated since they are determined from paths with as much as 40% of their length through tectonic regions other than cratons, should be large enough to compensate for effects related to neglecting azimuthal anisotropy.

Radial anisotropy may affect conclusions about isotropic shear velocity. Since Rayleigh waves constrain V_{SV} and are insensitive to V_{SH}, we must make assumptions about values of V_{SH} relative to V_{SV}. We plot and interpret Voigt-averaged isotropic shear velocity ($V_S = [2*V_{SV} + V_{SH}]/3$), and thus incorrect assumptions about V_{SH} may bias isotropic V_S. The values of V_{SH}-V_{SV} assumed for this study range from 0.08 km/s at 50 km depth to 0.15 km/s at 100 km to 0.04 km/s at 250 km. Global models of radial anisotropy show values for the cratonic mantle in the range 0–0.15 km/s at 50 km, 0.1–0.2 km/s at 100 km, and 0–0.1 km/s at 250 km [*Kustowski et al.*, 2008]. *Lebedev et al.* [2009] determined values of V_{SH}-V_{SV} in the Precambrian mantle lithosphere of approximately 0.14 km/s (i.e., 3%). Variations in observed radial anisotropy beneath cratons could thus result in

uncertainties in isotropic velocity as large as 0.03 km/s, although the uncertainties are likely to be <0.01 km/s at most locations (where the observed radial anisotropy is similar to our assumed value).

6.2. Constraints on the Temperature Structure of Cratons

In this paper, we use Rayleigh wave phase-velocity observations from cratons to identify a suite of 1-D Earth models whose elastic properties as a function of depth are consistent with the phase-velocity observations. This analysis directly constrains the range of elastic properties that characterize the cratonic upper mantle. We can use these elastic properties to investigate the thermal and chemical state of the cratonic upper mantle and evaluate the resulting temperature and compositional structures relative other data sets, for example the thermobarometric constraints provided by mantle xenoliths [e.g., *Rudnick et al.*, 1998; *Lee et al.*, 2011].

In this section we use the acceptable Earth models to draw inferences about the temperature structure in the cratonic upper mantle. To simplify the range of possible solutions, we fix mantle composition. We choose a peridotite composition that falls in the middle of the range spanned by Archean peridotites [*Lee et al.*, 2011] and can be considered representative of normal cratonic mantle as sampled by xenoliths. The prescribed major-element composition has the following values (wt %): $SiO_2 = 44.56\%$, $FeO = 7.39\%$, $MgO = 45.91\%$, $CaO = 0.87\%$, $Na_2O = 0.09\%$, and $Al_2O_3 = 1.17\%$, and $Mg\# = 92$ [$Mg\# = 100*MgO/(MgO + FeO)$ in molar fraction]. The software PerpleX [*Connolly*, 2009] is used to calculate shear velocity at 13,800 pressure-temperature combinations. Pressure is specified at 200 values from 0.1 to 20.0 GPa at increments of 0.1 GPa, and temperature is specified at 69 values from 25 to 1725°C at increments of 25°C. The calculation utilizes the database of thermodynamic and elastic properties of *Xu et al.* [2008]. To provide some context for the mineral abundance related to this composition, at a pressure corresponding to 150 km depth and temperature = 1100°C, PerpleX calculates that the stable assemblage is characterized by shear velocity = 4.61 km/s and consists of 76.1% olivine, 15.8% orthopyroxene, 4.2% clinopyroxene, and 3.9% garnet. This is similar to the compositions explored by, for example, *Bruneton et al.* [2004a] and *Darbyshire and Eaton* [2010]. Across the full range of temperatures and pressures the prescribed composition predicts a minimum shear velocity of 4.14 km/s at the lowest pressure and highest temperature and a maximum velocity of 6.09 km/s at the highest pressure and lowest temperature. Using this field of shear velocity, it is possible to convert a profile of shear velocity with depth into a profile of temperature with depth, assuming that 1 GPa = 30 km.

The shear-velocity calculation using PerpleX described above likely produces maximum velocity values, since the calculation ignores anelasticity, which reduces velocity at a given temperature [e.g., *Jackson et al.*, 2002], and is performed for a depleted composition, which elevates wave speed above the identical calculation performed for a fertile composition [e.g., *Lee*, 2003]. It therefore follows that the estimated upper mantle temperatures are also maximum values. Incorporating anelasticity or using a more fertile composition in the scaling from velocity to temperature would result in the inference of lower temperatures. We also note that this temperature-velocity scaling is different than the temperature-velocity scaling used to convert the geotherms to 1-D Earth models (section 3.1); in that case we use the anelastic parameterization of *Jackson and Faul* [2010] and test five different values of frequency and three different values of grain size. In converting the geotherms to Earth models, our objective was to generate velocity profiles that possess the general character (shape and magnitude) expected for continental temperature structure and include anelastic effects while also allowing for a very broad model-space search. For the conversion of shear velocity to temperature described in this section, we are utilizing thermodynamic calculations and available laboratory measurements on the elastic properties of upper mantle minerals, with the aim of trying to more accurately place an upper bound on temperature in the cratonic upper mantle.

In Figure 11a we show estimated upper mantle temperatures for the four average profiles obtained by applying cluster analysis to the a posteriori models for the 37–400 km depth-range scenario (Figure 10c). As expected, a maximum in wave speed produces a minimum in temperature, and a positive gradient of velocity with depth produces a negative gradient of temperature with depth. The group 2 and group 4 profiles, which contain positive velocity gradients at depths <150 km, show decreasing or constant temperature with depth to 150 km. The group 1 and group 3 profiles show positive temperature gradients to depths of 250–300 km. All four of the profiles are colder than the temperature estimates from cratonic xenoliths at depths >100 km. The group 3 profile tracks the coldest xenoliths from 75 to 200 km. As a result of the LVZ
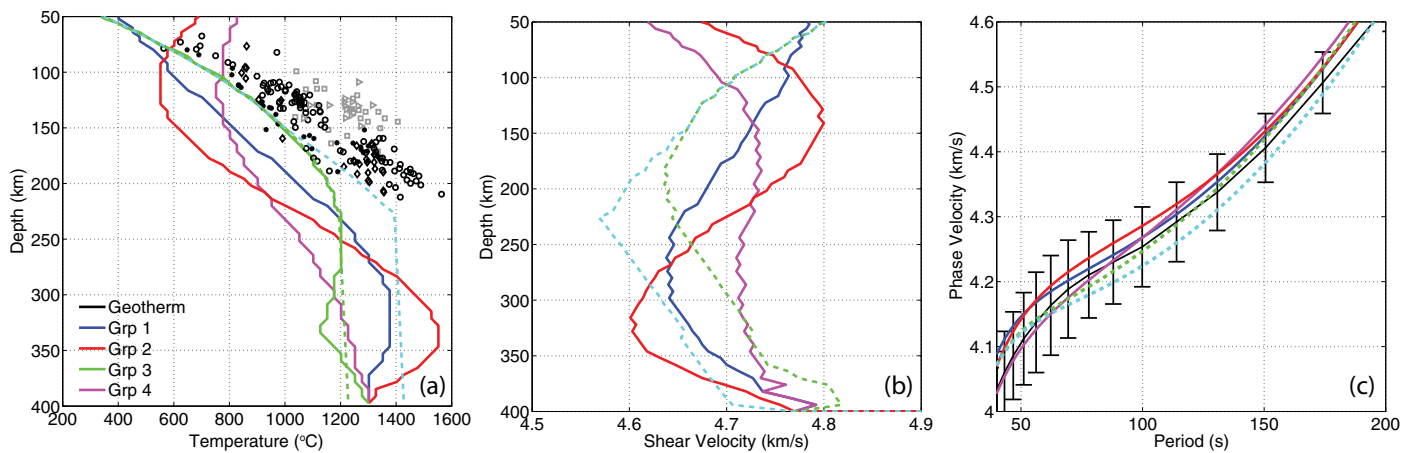
Figure 11. (a) Colored curves show temperature profiles estimated from the four average profiles determined from cluster analysis for the 37–400 km depth-range scenario (Figure 10c). The procedure for scaling isotropic shear velocity to temperature is described in the text. The dashed green curve follows the group 3 profile at depths <250 km and an adiabatic temperature gradient (0.2°C/km) at greater depths. The dashed cyan curve follows the group 3 profile at depths <170 km, tracks the coldest xenoliths to 225 km depth, and is adiabatic at greater depths. Black symbols show P-T values obtained from mantle xenoliths from cratons in South Africa (circles), Siberia (diamonds), and Slave (stars). Gray symbols are from xenoliths in Tanzania (squares) and the Colorado Plateau (triangles). (b) Isotropic shear-velocity profiles predicted from temperature profiles in Figure 11a. The group 3 profile is not shown, as it overlaps almost entirely with the dashed green curve. (c) Rayleigh wave phase velocity predicted for the five models in Figure 11b and compared to the observed range for cratons.

in the group 3 velocity profile at 200 km, the group 3 temperatures at greater depths approximately follow a mantle adiabat (i.e., nearly constant temperature with depth), which is colder by 100–200°C than the mantle adiabat that would be inferred from the xenolith P-T constraints. We have confirmed that the LVZ at 200 km in the group 3 profile is not an artifact introduced by our requirement that the randomly generated models rejoin STW105 at 400 km, since the group 3 profile for the 37–500 km depth-range scenario is nearly identical (Figure 10d).

The dashed green curve in Figure 11a shows a temperature structure with a similar shape as that inferred from the group 3 profile; however, at depths >250 km we have prescribed adiabatic temperature with a gradient of 0.2°C/km. Since these temperatures are clearly colder than those obtained from the cratonic xenoliths, we also investigate a temperature structure, shown by the dashed cyan curve, that is identical at depths <170 km, tracks the coldest xenoliths to 225 km depth, and is adiabatic at greater depths. Both temperature profiles are converted into isotropic shear velocity using the scaling approach described above. Figure 11b compares them to the profiles obtained through cluster analysis; comparison of Figures 11a and 11b helps to illustrate how the joining of the conductive and adiabatic layers results in a low-velocity zone. The blue, red, green, and magenta curves in Figure 11b are essentially identical to the curves in Figure 10c; their jaggedness results from using a temperature-velocity scaling that is parameterized every 25°C and 0.1 GPa. All five Earth models (solid lines: three profiles from cluster analysis; dashed lines: two idealized temperature structures) have the same 37 km Archean crust as described in section 3. In order to maximize the predicted phase velocity, the ratio $V_P/V_S = 1.85$ at depths 37–400 km. All parameters in the Earth model are identical to STW105 at depths >400 km.

Figure 11c compares the corresponding phase-velocity predictions to the observed range. While all five sets of predictions fall within the observed phase-velocity range, Figure 11c helps to highlight the strengths and weaknesses of the various models. The three models with a negative velocity gradient and positive temperature gradient (i.e., the group 1 profile plus the two idealized temperature structures from Figure 11a) cannot match the observed steep increase of phase velocity with period; this is consistent with the acceptable geotherm-generated models (Figure 6c). On the other hand, the group 2 and group 4 profiles, which have positive velocity gradients at shallow depths, more closely match the shape of the observed phase-velocity curves. However, the temperature structures inferred from the group 2 and group 4 profiles require temperatures that increase more gradually with depth and that are colder than the xenoliths by >200°C to depths >200 km. Positive temperature gradients with depth that are as strong as those defined by the xenolith data set will necessarily be accompanied by strong shear-velocity gradients, with high velocities underlain by low velocities underlain by high velocities (Figure 11b). Since Rayleigh waves at a given period are sensitive over a range of depths, the net effect is fairly constant phase velocity in the period range 40–80 s,

which is not consistent with the steep increase with period that defines center of the observed phase-velocity range.

The final conclusion from Figure 11 is that a shear-velocity profile derived from a temperature structure that is consistent with only the coldest xenoliths (i.e., the dashed cyan curve) is essentially inconsistent with the Rayleigh wave observations. While the predicted phase velocity falls within the observed range, it is slower the majority of the observations (e.g., Figures 2b and 3b), and the use of $V_P/V_S = 1.85$, purely elastic velocity, and a depleted composition all work to maximize phase velocity. Relaxing any of these parameters, or considering a warmer geotherm that better overlaps with the xenolith thermobarometry, will decrease phase velocity and push the predicted values outside of the observed range.

We therefore conclude that it is difficult to simultaneously satisfy xenolith and surface-wave constraints on cratonic temperature structure. If the xenolith thermobarometry and the elastic constants used for the velocity calculation are assumed to be robust, then it seems likely that the assumption of a depleted peridotite composition for the entire cratonic upper mantle is not appropriate. This outcome agrees with the conclusions reached by *Bruneton et al.* [2004a] for the Baltic Shield and *Pedersen et al.* [2009] for Yilgarn, Slave, and South-Central Finland. Bringing the xenolith-derived velocity profile (dashed cyan curve in Figure 11) into agreement with the phase-velocity observations requires reducing shear velocity in the shallowest mantle (i.e., periods <60 s) and increasing it at greater depths (i.e., periods 60–175 s). For the Baltic Shield, *Bruneton et al.* [2004a] proposed a stratified mantle lithosphere, with anomalous and seismically slow material overlying normal cratonic peridotite. *Pedersen et al.* [2009] considered 5–6% phlogopite in the uppermost mantle but ruled it out based on lack of evidence in xenolith suites, and *Lebedev et al.* [2009] proposed a broad spinel-to-garnet transition field. These latter two studies did not consider in a quantitative way the effect of temperature on the seismic profiles. Anomalous and slow material in the shallowest mantle would help to reconcile our discrepancy at short periods, but at longer periods we need a means of increasing shear velocity relative to normal cratonic peridotite, which was used for the calculations shown in Figure 11. Future work will consider adjustments to the mantle composition, for example increasing the amount of garnet or eclogite, which can help to reconcile the discrepancy between xenolith and seismological observations. Future work will also consider individual cratonic settings separately.

7. Conclusions

In this study we identified a suite of 1-D Earth models whose elastic properties as a function of depth predict Rayleigh wave phase velocities that are consistent with observations of phase velocity for Rayleigh waves propagating through Precambrian cratons. Our goal is to characterize the average global seismic properties of cratons. The 1-D Earth models were created using two separate approaches. Geotherm-generated models contain shear velocity that is predicted from 1-D temperature profiles. A large and realistic range of surface heat flow and lithospheric heat-production values are used for the temperature calculations and 15 different temperature-velocity scalings are tested. Randomly generated models contain shear velocity that is calculated by randomly perturbing the global reference model STW105 [*Kustowski et al.*, 2008] in four different depth ranges.

Our analysis shows that it is possible to find geotherm-generated Earth models that are consistent with the observations. These models contain a distinct low-velocity zone at approximately 175 km depth. The 165 acceptable models are highly similar to one another. Prescribing a lower V_P/V_S ratio in the mantle permits a larger number of acceptable models, which are more variable and are characterized by higher isotropic shear velocity and slightly shallower low-velocity zones. However, for both low and high V_P/V_S ratios the shape of the geotherm-generated dispersion curves is fundamentally different than the shape of the observed dispersion curves, making the model-selection criterion highly sensitive to width of the observed phase-velocity range. Thus, while our analysis identifies geotherm-generated models that satisfy the observations, we must also note that many of the acceptable Earth models would be disqualified if a smaller width were used to define the observed range.

We show that it is possible to find randomly generated Earth models with high velocities confined to depths <200 km that are consistent with the observations. The isotropic shear velocity for these models is quite high—higher by 0.4 km/s than STW105 and by 0.2 km/s than regional seismic studies—and all of the models contain a positive velocity gradient with depth in the depth range 50–100 km. Taking this result at

face value indicates that the fundamental-mode Rayleigh wave phase velocities in the period range 40–235 s permit the high-velocity lid beneath cratons to be relatively thin.

When the random perturbations are allowed to extend to 300, 400, or 500 km, the shear velocities are higher than STW105 by approximately 0.2 km/s. For these three depth-range scenarios, the acceptable models merge with the global average at 300 km depth, indicating that 300 km is a reasonable value for the thickness of the high-velocity lid beneath cratons. At this stage we are not assigning this value as the thickness of the cratonic lithosphere, since inferring a rheological lithosphere from seismological properties is not straightforward [e.g., *Eaton et al.*, 2009]. For these models, the velocity gradients with depth in the depth range 50–100 km are neither strongly positive nor strongly negative; most models contain roughly constant shear velocity with depth in the shallow mantle lithosphere.

The relatively large standard deviation values that we use to characterize the width of the observed range of cratonic phase velocity permit a wide range of shear-velocity profiles and, correspondingly, a wide range of temperature profiles. However, essentially all of the acceptable randomly generated models predict temperature profiles that are colder (when assuming a uniform depleted peridotite composition) than the temperatures indicated by cratonic peridotite xenoliths. It is difficult to find a temperature structure that can simultaneously match the xenolith and phase-velocity observations. This is true even when we try to optimize the agreement, for example by fitting only the coldest of the xenoliths and by prescribing a very high V_P/V_S ratio. Future work to resolve this discrepancy must consider assumptions inherent to each type of analysis, for example to what extent the xenoliths can be considered representative of present-day mantle conditions and whether the scaling between temperature and seismic velocity must consider compositions other than peridotite.

References

Afonso, J. C., G. Ranalli, M. Fernandez, W. L. Griffin, S. Y. O'Reilly, and U. Faul (2010), On the Vp/Vs-Mg# correlation in mantle peridotites: Implications for the identification of thermal and compositional anomalies in the upper mantle, *Earth Planet. Sci. Lett.*, *289*, 606–618, doi:10.1016/j.epsl.2009.12.005.

Afonso, J. C., J. Fullea, W. L. Griffin, Y. Yang, G. Jones, J. A. D. Connolly, and S. Y. O'Reilly (2013a), 3-D multiobservable probabilistic inversion for the composition and thermal structure of the lithosphere and upper mantle: 1. A priori petrological information and geophysical observables, *J. Geophys. Res. Solid Earth*, *118*, 2586–2617, doi:10.1002/jgrb.50124.

Afonso, J. C., J. Fullea, Y. Yang, J. A. D. Connolly, and A. G. Jones (2013b), 3-D multi-observable probabilistic inversion for the compositional and thermal structure of the lithosphere and upper mantle: 2. General methodology and resolution analysis, *J. Geophys. Res. Solid Earth*, *118*, 1650–1676, doi:10.1002/jgrb.50123.

Bassin, C., G. Laske, and G. Masters (2000), The current limits of resolution for surface wave tomography in North America, *Eos Trans. AGU*, *81*, F897.

Boyd, F. R., N. P. Pokhilenko, D. G. Pearson, S. A. Mertzman, N. V. Sobolev, and L. W. Finger (1997), Composition of the Siberian cratonic mantle: Evidence from Udachnaya peridotite xenoliths, *Contrib. Mineral. Petrol.*, *128*, 228–246, doi:10.1007/s004100050305.

Bruneton, M., H. A. Pedersen, P. Vacher, I. T. Kukkonen, N. T. Arndt, S. Funke, W. Friederich, and V. Farra (2004a), Layered lithospheric mantle in the central Baltic shield from surface waves and xenolith analysis, *Earth Planet. Sci. Lett.*, *226*, 41–52, doi:10.1016/j.epsl.2004.07.034.

Bruneton, M., et al. (2004b), Complex lithospheric structure under the central Baltic shield from surface wave tomography, *J. Geophys. Res.*, *109*, B10303, doi:10.1029/2003JB002947.

Carlson, R. W., D. G. Pearson, and D. E. James (2005), Physical, chemical, and chronological characteristics of continental mantle, *Rev. Geophys.*, *43*, RG1001, doi:10.1029/2004RG000156.

Chen, C.-W., S. Rondenay, D. S. Weeraratne, and D. B. Snyder (2007), New constraints on the upper mantle structure of the Slave craton from Rayleigh wave inversion, *Geophys. Res. Lett.*, *34*, L10301, doi:10.1029/2007GL029535.

Connolly, J. A. D. (2009), The geodynamic equation of state: What and how, *Geochem. Geophys. Geosyst.*, *10*, Q10014, doi:10.1029/2009GC002540.

Dalton, C. A., C. H. Langmuir, A. Gale (2014), Geophysical and geochemical evidence for deep temperature variations beneath mid-ocean ridges, *Science*, *344*, 6179, 80–83, doi:10.1126/science.1249466.

Dalton, C. A., and U. H. Faul (2010), The oceanic and cratonic upper mantle: Clues from joint interpretation of global velocity and attenuation models, *Lithos*, *120*, 160–172, doi:10.1016/j.lithos.2010.08.020.

Darbyshire, F. A., and D. W. Eaton (2010), The lithospheric root beneath Hudson Bay, Canada from Rayleigh wave dispersion: No clear seismological distinction between Archean and Proterozoic mantle, *Lithos*, *120*, 144–159, doi:10.1016/j.lithos.2010.04.010.

Darbyshire, F. A., D. W. Eaton, A. W. Frederiksen, and L. Ertolahti (2007), New insights into the lithosphere beneath the superior province from Rayleigh wave dispersion and receiver function analysis, *Geophys. J. Int.*, *169*, 1043–1068, doi:10.1111/j.1365-246X.2006.03259.x.

Dziewonski, A. M., and D. L. Anderson (1981), Preliminary reference Earth model, *Phys. Earth Planet. Inter.*, *25*, 297–356.

Eaton, D. W., F. Darbyshire, R. L. Evans, H. Grutter, A. G. Jones, and X. Yuan (2009), The elusive lithosphere-asthenosphere boundary (LAB) beneath cratons, *Lithos*, *109*, 1–22, doi:10.1016/j.lithos.2008.05.009.

Ekström, G. (2011), A global model of Love and Rayleigh surface wave dispersion and anisotropy, 25-250 *s*, *Geophys. J. Int.*, *187*, 1668–1686, doi:10.1111/j.1365-246x.2011.05225.x.

Faul, U. H., and I. Jackson (2005), The seismological signature of temperature and grain size variations in the upper mantle, *Earth Planet. Sci. Lett.*, *234*, 119–134, doi:10.1016/j.epsl.2005.02.008.

Fishwick, S., and A. M. Reading (2008), Anomalous lithosphere beneath the Proterozoic of western and central Australia: A record of continental collision and intraplate deformation?, *Precambrian Res.*, *166*, 111–121, doi:10.1016/j.precamres.2007.04.026.

Fishwick, S., B. L. N. Kennett, and A. M. Reading (2005), Contrasts in lithospheric structure within the Australian craton-insights from surface wave tomography, *Earth Planet. Sci. Lett.*, *231*, 163–176, doi:10.1016/j.epsl.2005.01.009.

French, S., V. Lekic, and B. Romanowicz (2013), Waveform tomography reveals channeled flow at the base of the oceanic asthenosphere, *Science*, *342*(6155), 227–230, doi:10.1126/science.1241514.

Gaherty, J. B., and R. A. Dunn (2007), Evaluating hot spot-ridge interaction in the Atlantic from regional-scale seismic observations, *Geochem. Geophys. Geosyst.*, *8*, Q05006, doi:10.1029/2006GC001533.

Goes, S., R. Govers, and P. Vacher (2000), Shallow mantle temperature under Europe from P and S wave tomography, *J. Geophys. Res.*, *105*, 11,153–11,169, doi:10.1029/1999JP900300.

Hieronymus, C. F., and S. Goes (2010), Complex cratonic seismic structure from thermal models of the lithosphere: Effects of variations in deep radiogenic heating, *Geophys. J. Int.*, *180*, 999–1012, doi:10.111/j.1365-246X.2009.04478.x.

Hirth, G., R. L. Evans, and A. D. Chave (2000), Comparison of continental and oceanic upper mantle electrical conductivity: Is the Archean lithosphere dry?, *Geochem. Geophys. Geosyst.*, *1*, 1030, doi:10.1029/2000GC000048.

Jackson, I., and U. H. Faul (2010), Grainsize-sensitive viscoelastic relaxation in olivine: Towards a robust laboratory-based model for seismological application, *Phys. Earth Planet. Inter.*, *183*, 151–163, doi:10.1016/j.pepi.2010.09.005.

Jackson, I., J. D. Fitz Gerald, U. H. Faul, and B. H. Tan (2002), Grain-size-sensitive seismic wave attenuation in polycrystalline olivine, *J. Geophys. Res.*, *107*(B12), 2360, doi:10.1029/2001JF001225.

Jaupart, C., and J. C. Mareschal (1999), The thermal structure and thickness of continental roots, *Lithos*, *48*, 93–114, doi:10.1016/s0024-4937(99)00023-7.

Jordan, T. H. (1975), Continental tectosphere, *Rev. Geophys.*, *13*, 1–12, doi:10.1029/RG013i003p00001.

Jordan, T. H. (1978), Composition and development of continental tectosphere, *Nature*, *274*, 544–548, doi:10.1038/274544a0.

Jordan, T. H. (1979), Mineralogies, densities and seismic velocities of garnet lherzolite and their geophysical implications, in *The Mantle Sample: Inclusions in Kimberlites and Other Volcanics*, edited by F. R. Boyd and H. O. A. Meyer, pp. 1–14, AGU, Washington, D. C.

Jordan, T. H. (1981), Global tectonic regionalization for seismological data analysis, *Bull. Seismol. Soc. Am.*, *71*, 1131–1141.

Jordan, T. H., and E. M. Paulson (2013), Convergence depths of tectonic regions from an ensemble of global tomographic models, *J. Geophys. Res. Solid Earth*, *118*, 4196–4225, doi:10.1002/jgrb.50263.

Khan, A., L. Boschi, and J. A. D. Connolly (2011), Mapping the Earth's thermochemical and anisotrophic structure using global surface wave data, *J. Geophys. Res.*, *116*, B01301, doi:10.1029/2010JB007828.

Kopylova, M. G., and J. K. Russell (2000), Chemical stratification of cratonic lithosphere: Constraints from northern Slave craton, Canada, *Earth Planet. Sci. Lett.*, *181*, 71–87, doi:10.1016/S0012-821X(00)00187-4.

Kustowski, B., G. Ekström, and A. M. Dziewonski (2008), Anisotropic shear-wave velocity structure of the Earth's mantle: A global model, *J. Geophys. Res.*, *113*, B06306, doi:10.1029/2007JB005169.

Larson, A. M., J. A. Snoke, and D. E. James (2006), S-wave velocity structure, mantle xenoliths and the upper mantle beneath the Kaapvaal craton, *Geophys. J. Int.*, *167*, 171–186, doi:10.1111/j.1365-246X.2006.03005.x.

Laske, G., G. Masters, Z. Ma, and M. Pasyanos (2013), Update on CRUST1.0—A 1-degree global model of Earth's crust, *Geophys. Res. Abstr.*, *15*, 2658.

Lebedev, S., J. Boonen, and J. Trampert (2009), Seismic structure of Precambrian lithosphere: New constraints from broad-band surface-wave dispersion, *Lithos*, *109*, 96–111, doi:10.1016/j.lithos.2008.06.010.

Lee, C.-T. A. (2003), Compositional variation of density and seismic velocities in natural peridotites at STP conditions: Implications for seismic imaging of compositional heterogeneities in the upper mantle, *J. Geophys. Res.*, *108*(B9), 2441, doi:10.1029/2003JB002413.

Lee, C.-T. A., P. Luffi, and E. J. Chin (2011), Building and destroying continental mantle, *Annu. Rev. Earth Planet. Sci.*, *39*, 59–90, doi:10.1146/annurev-earth-040610-133505.

Lekic, V., and B. Romanowicz (2011a), Inferring upper-mantle structure by full waveform tomography with the spectral element method, *Geophys. J. Int.*, *185*, 799–831, doi:10.111/j.1365-246X.2011.04969.x.

Lekic, V., and B. Romanowicz (2011b), Tectonic regionalization without a priori information: A cluster analysis of upper mantle tomography, *Earth Planet. Sci. Lett.*, *308*, 151–160, doi:10.1016/j.epsl.2011.05.050.

Li, A., and K. Burke (2006), Upper mantle structure of southern Africa from Rayleigh wave tomography, *J. Geophys. Res.*, *111*, B10303, doi:10.1029/2006JB004321.

Mareschal, J.-C., and C. Jaupart (2013), Radiogenic heat production, thermal regime and evolution of continental crust, *Tectonophysics*, *609*, 524–534, doi:10.1016/j.tecto.2012.12.001.

Nishimura, C. E., and D. W. Forsyth (1989), The anisotropic structure of the upper mantle in the Pacific, *Geophys. J. Int.*, *96*, 203–229, doi:10.111/j.1365-246X.1989.tb04446.x.

Nyblade, A. A., and H. N. Pollack (1993), A global analysis of heat flow from Precambrian terrains: Implications for the thermal structure of Archean and Proterozoic lithosphere, *J. Geophys. Res.*, *98*, 12,207–12,218, doi:10.1029/93JB00521.

Panning, M., and B. Romanowicz (2006), A three-dimensional radially anisotropic model of shear velocity in the whole mantle, *Geophys. J. Int.*, *167*, 361–379, doi:10.1111/j.1365-246X.2006.03100.x.

Pedersen, H. A., S. Fishwick, and D. B. Snyder (2009), A comparison of cratonic roots through consistent analysis of seismic surface waves, *Lithos*, *109*, 81–95, doi:10.1016/j.lithos.2008.09.016.

Priestley, K., D. McKenzie, and E. Debayle (2006), The state of the upper mantle beneath southern Africa, *Tectonophysics*, *416*, 101–112, doi:10.1016/j.tecto.2005.11.024.

Ritsema, J., A. Deuss, H. J. van Heijst, and J. H. Woodhouse (2011), S40RTS: A degree-40 shear-velocity model for the mantle from new Rayleigh wave dispersion, teleseismic travel time and normal-mode splitting function measurements, *Geophys. J. Int.*, *184*, 1223–1236, doi:10.1111/j.1365-246X.2010.04884.x.

Rudnick, R. L., and D. M. Fountain (1995), Nature and composition of the continental crust: A lower crustal perspective, *Rev. Geophys.*, *33*, 267–309, doi:10.1029/95RG01302.

Rudnick, R. L., and A. A. Nyblade (1999), The thickness and heat production of Archean lithosphere: Constraints from xenolith thermobarometry and surface heat flow, *Spec. Publ. Geochem. Soc.*, *6*, 3–12.

Rudnick, R. L., W. F. McDonough, and R. J. O'Connell (1998), Thermal structure, thickness, and composition of continental lithosphere, *Chem. Geol.*, *145*, 395–411.

Rychert, C. A., and P. M. Shearer (2009), A global view of the lithosphere-asthenosphere boundary, *Science*, *324*, 495–498, doi:10.1126/science.1169754.

Schutt, D. L., and C. E. Lesher (2006), Effects of melt depletion on the density and seismic velocity of garnet and spinel lherzolite, *J. Geophys. Res.*, *111*, B05401, doi:10.1029/2003JB002950.

Shan, B., J. C. Afonso, Y. Yang, C. J. Grose, Y. Zheng, X. Xiong, and L. Zhou (2014), The thermochemical structure of the lithosphere and upper mantle beneath south China: Results from multiobservable probabilistic inversion, *J. Geophys. Res. Solid Earth*, *119*, 8417–8441, doi:10.1002/2014JB011412.

Shapiro, N. M., and M. H. Ritzwoller (2004), Thermodynamic constraints on seismic inversions, *Geophys. J. Int.*, *157*, 1175–1188, doi:10.1111/j.1365-246X.2004.02254.x.

Shapiro, N. M., M. H. Ritzwoller, J. C. Mareschal, and C. Jaupart (2004), Lithospheric structure of the Canadian shield inferred from inversion of surface-wave dispersion with thermodynamic a priori constraints,: *Geological Prior Information: Informing Science and Engineering*, *Geol. Soc. Spec. Publ.*, *239*, edited by A. Curtis and R. Wood, 175–194.

Shapiro, S. S., B. H. Hager, and T. H. Jordan (1999), The continental tectosphere and Earth's long-wavelength gravity field, *Lithos*, *48*, 135–152, doi:10.1016/S0024-4937(99)00027-4.

Stixrude, L., and C. Lithgow-Bertelloni (2005), Mineralogy and elasticity of the oceanic upper mantle: Origin of the low-velocity zone, *J. Geophys. Res.*, *110*, B03204, doi:10.1029/2004JB002965.

Weeraratne, D. S., D. W. Forsyth, and K. M. Fischer (2003), Evidence for an upper mantle plume beneath the Tanzanian craton from Rayleigh wave tomography, *J. Geophys. Res.*, *108*(B9), 2427, doi:10.1029/2002JB002273.

Xu, W., C. Lithgow-Bertelloni, L. Stixrude, and J. Ritsema (2008), The effect of bulk composition and temperature on mantle seismic structure, *Earth Planet. Sci. Lett.*, *275*, 70–79, doi:10.1016/j.epsl.2008.08.012.

Yang, Y., D. W. Forsyth, and D. S. Weeraratne (2007), Seismic attenuation near the East Pacific Rise and the origin of the low-velocity zone, *Earth Planet. Sci. Lett.*, *258*, 260–268, doi:10.1016/j.epsl.2007.03.040.

Yuan, H., and B. Romanowicz (2010), Lithospheric layering in the North American craton, *Nature*, *466*, 1063–1069, doi:10.1038/nature09332.

Yuan, H., S. French, P. Cupillard, and B. Romanowicz (2014), Lithospheric expression of geological units in central and eastern North America from full waveform tomography, *Earth Planet. Sci. Lett.*, *402*, 176–186, doi:10.1016/j.epsl.2013.11.057.

Zhu, H., and J. Tromp (2013), Mapping tectonic deformation in the crust and upper mantle beneath Europe and the north Atlantic ocean, *Science*, *341*, 871–875, doi:10.1126/science.1241335.